












## RESEARCH ARTICLE

# Targeting TUBG1 in RB1-negative tumors

Lisa Lindström<sup>1</sup>  | Jingkai Zhou<sup>1</sup>  | Bruno O. Villoutreix<sup>2</sup>  | Darina Malycheva<sup>1</sup> |  
 Magdalena Otrocka<sup>3</sup>  | Anna-Lena Gustavsson<sup>3</sup>  | Thomas Lundbäck<sup>3</sup>  |  
 David Bliman<sup>4</sup>  | Muhammad Anwar Shameem<sup>4</sup>  | Megan Straw<sup>5</sup> |  
 Kristian Riesbeck<sup>5</sup>  | Roger Olsson<sup>4,6</sup>  | Maria Alvarado-Kristensson<sup>1</sup> 

<sup>1</sup>Molecular Pathology, Department of Translational Medicine, Lund University, Malmö, Sweden<sup>2</sup>Université Paris Cité, Inserm, NeuroDiderot, Paris, France<sup>3</sup>Chemical Biology Consortium Sweden, Science for Life Laboratory, Karolinska Institutet, Solna, Sweden<sup>4</sup>Department of Chemistry and Molecular Biology, University of Gothenburg, Gothenburg, Sweden<sup>5</sup>Clinical Microbiology, Department of Translational Medicine, Lund University, Malmö, Sweden<sup>6</sup>Chemical Biology & Therapeutics, Department of Experimental Medical Science, Lund University, Lund, Sweden**Correspondence**

Maria Alvarado-Kristensson, Molecular Pathology, Lund University, 53 Inga Marie Nilssons Street, Floor 2, Malmö SE-214 28, Sweden.  
 Email: [maria.alvarado-kristensson@med.lu.se](mailto:maria.alvarado-kristensson@med.lu.se)

**Funding information**

Cancerfonden (Swedish Cancer Society), Grant/Award Number: 22 2176Pj; Barncancerfonden (Swedish Childhood Cancer Foundation), Grant/Award Number: PR2022-0058; BioCare, Grant/Award Number: 2012; Novo Nordisk foundation, Grant/Award Number: 12759; Skane University Hospital in Malmö Cancer Research, Grant/Award Number: 2022; Sten K Johnsons stiftelse (Sten K Johnson Foundation), Grant/Award Number: 2022; MultiPark (the Lund University Strategic Research Areas), Grant/Award Number: N/A; Swedish Research Council, Grant/Award Number: 2021-00179; SciLifeLab, Grant/Award Number: N/A

**Abstract**

The disruption of microtubule dynamics serves as a pivotal strategy for eliminating tumor cells, despite its accompanying toxicities affecting non-tumor cells. This study investigates the potential of selectively targeting  $\gamma$ -tubulin1 (TUBG1) as a therapeutic strategy in cancer treatment. By elucidating the TUBG1–E2F1–retinoblastoma protein (RB1) network, we introduce a novel compound, 4-(6-((3-Methoxyphenyl)amino)pyrimidin-4-yl)-N,N-dimethylbenzenamine, (L12). L12 treatment enhanced RB1 expression and selectively targeted cells with impaired RB1 signaling, while reduced E2F1 expression attenuated its cytotoxicity. Furthermore, L12-mediated cytotoxicity depends on an E2F1-mediated upregulation of procaspase 3 expression, highlighting the role of E2F1 in the apoptotic response. Unlike traditional tubulin-targeting agents, L12's specificity for tumor cells lies in its inhibitory effects on TUBG1, without affecting the second human isoform of TUBGs, TUBG2. Despite its interaction with specific kinases, the concentrations required for antitumor effects are 100-fold lower than those influencing kinase activities. Subsequent investigations underscore L12's reduced neuronal axonal toxicity compared to vincristine. Lastly, L12 demonstrates promising results in inhibiting tumor growth in xenografted small cell lung cancer models, demonstrating potential specificity toward tumor cells while minimizing adverse effects on healthy tissues. This research emphasizes the potential of

Lisa Lindström and Jingkai Zhou contributed equally to this work.

This is an open access article under the terms of the [Creative Commons Attribution-NonCommercial-NoDerivs](https://creativecommons.org/licenses/by-nc-nd/4.0/) License, which permits use and distribution in any medium, provided the original work is properly cited, the use is non-commercial and no modifications or adaptations are made.

© 2025 The Author(s). *The FASEB Journal* published by Wiley Periodicals LLC on behalf of Federation of American Societies for Experimental Biology.

TUBG1 inhibitors as a promising advancement in personalized chemotherapy approaches and their potential as a groundbreaking treatment for various cancers.

#### KEYWORDS

cancer, chemotherapy, RB1, TUBG1

## 1 | INTRODUCTION

Disrupting the dynamics of microtubules is a frequently employed strategy to eliminate tumor cells. These drugs, whether stabilizing or destabilizing microtubules, disrupt mitotic spindle formation and chromosome partitioning, leading to cell death. They are widely prescribed antineoplastic drugs for treating malignancies, including lung, breast, gastric, esophageal, bladder, and prostate cancer, Kaposi sarcoma, and squamous cell carcinoma of the head and neck.<sup>1</sup> Unfortunately, the treatment causes acute and long-term toxicities, significantly impacting long-term survivors, as it also affects non-tumor cells.<sup>1</sup>

Microtubules consist of two members of the GTPase superfamily of tubulins:  $\alpha$ -tubulin and  $\beta$ -tubulin. A third member,  $\gamma$ -tubulin (TUBG), is a ubiquitously expressed protein and the core component of the cytoskeleton/nucleoskeleton named the  $\gamma$ -tubulin meshwork.<sup>2–5</sup> TUBG, in conjunction with  $\gamma$ -tubulin complex proteins (GCPs), plays a pivotal role as a nucleator of microtubules. These complexes initiate microtubule assembly from centrosomes and other membranous structures within the cells.<sup>5,6</sup> In humans, several genes encode  $\alpha$ -tubulin and  $\beta$ -tubulin, while there are two encoding TUBG: *TUBG1* and *TUBG2*.<sup>7</sup> Mutations in the *TUBG1* gene have been found to cause brain malformations.<sup>8</sup>

The self-polymerizing ability of TUBG results in the interlinking of the components of the  $\gamma$ -tubulin meshwork, that is,  $\gamma$ -tubules,  $\gamma$ -strings, and centrosomes.<sup>2,3,9–12</sup> We discovered that nuclear TUBG binds to and moderates the activities of E2 promoter-binding factor (E2F). Inhibition of the TUBG activities leads to an E2F1-mediated increase in retinoblastoma protein (RB1) levels,<sup>13,14</sup> implying that TUBG and RB1 inversely moderate each other's expression by directly binding to E2F-binding sites on *TUBG* and *RB1* promoter regions.<sup>13</sup> Notably, reduced TUBG protein levels also enhance E2F1-mediated expression of procaspase 3, indicating a broader regulatory role for TUBG in cell survival pathways.<sup>13</sup> In various tumor types and cell lines, there is an inverse correlation between the expression levels of TUBG and RB1, and impairment of the activities of TUBG kills tumor cells with a distorted RB1-signal pathway,<sup>13,15,16</sup> highlighting the nuclear activity of TUBG as a strategy for targeted chemotherapy of RB1-deficient tumors.

Based on the TUBG–E2F–RB1 network, inhibition of TUBG increases the E2F activities.<sup>14</sup> Applying this strategy, citral dimethyl acetal (CDA) was described as the first inhibitor of the nuclear activities of TUBG.<sup>16,17</sup> CDA binds to the GTP-binding domain of TUBG, interfering with its GTPase activity.<sup>18</sup> Furthermore, CDA is a  $\gamma$ -tubule depolymerizing agent.<sup>2</sup> Due to the lack of options among inhibitors that target the nuclear activity of TUBG, we employed an E2F-based luciferase-screening assay and used various compound libraries to discover novel inhibitors that interfere with this activity. We report here the discovery of the compound 4-((3-Methoxyphenyl)amino)pyrimidin-4-yl)-N,N-dimethylbenzenamine (L12). This compound functions as a  $\gamma$ -tubule polymerizing agent and enhances the expression of RB1. In vitro, L12 kills tumor cells carrying defects in the RB1 signaling pathway. Furthermore, when comparing cells expressing TUBG1 to those expressing TUBG2, we observed that L12 induces the highest level of cell death in cells with TUBG1 expression. Finally, we provide evidence of L12's in vivo antitumor activity.

## 2 | MATERIALS AND METHODS

### 2.1 | Chemicals and reagents

The following antibodies and reagents were utilized in the study: anti-RB1 (1:200; cat. No. sc-74562, [RRID:AB\\_2177334](#)), anti-phosphorylated Ser<sup>780</sup> RB1 (1:200; cat. No. sc-12901, [RRID:AB\\_655237](#)), anti-histone H3 (1:1000; cat. No. sc-517576, [RRID:AB\\_2848194](#)), anti- $\beta$ 3-tubulin (1:2000; cat. No. sc-80005, [RRID:AB\\_2210816](#)), anti-E2F1 (1:500; cat. No. sc-251, [RRID:AB\\_627476](#)), anti-procaspase 3 (1:500; cat. No. sc-98785, [RRID:AB\\_2069883](#)), and anti-GAPDH (1:5000; cat. No. sc-47724, [RRID:AB\\_627678](#)) from Santa Cruz Biotechnology; anti-TUBG (1:500 mouse, cat. No. T6557, [RRID:AB\\_477584](#), and 1:400 rabbit, cat. No. T3320, [RRID:AB\\_261655](#)), anti-Flag (1:200; cat. No. F7425, [RRID:AB\\_439687](#)), anti-actin (1:600; cat. No. A5441, [RRID:AB\\_476744](#)), anti-mouse IgG-HRP linked F(ab')<sub>2</sub> fragment (1:6000; cat. No. GENA9310), and anti-rabbit IgG-HRP linked (1:6000; cat. No. GENA934, [RRID:AB\\_2722659](#)) from Merck life Science; anti- $\alpha$ -tubulin (1:400; cat. No. CP06, [RRID:AB\\_2617116](#)).

from Calbiochem; SDS-PAGE reagents (Bio-Rad); donkey anti-mouse (1:1400) or anti-rabbit (1:1400) Alexa fluor 488 or Cyanine Cy3 conjugated (Jackson, cat. No.: 715-005-150 [RRID:AB\_2340758], 711-005-152 [RRID:AB\_2340585], 715-545-150 [RRID:AB\_2340846] and 711-545-152 [RRID:AB\_2313584]). All other reagents were obtained from Merck life Science.

The anti-TUBG antibodies recognized the following TUBG sequences: T3320, raised against amino acids at the C-terminus of *Xenopus* TUBG, and T6557, raised against amino acids 38–53 at the N-terminus of TUBG.

Human *TUBG1* singleguide (sg; RRID:Addgene\_104437) and short hairpin (sh) RNA (RRID:Addgene\_87955), human sg-resistant pcDNA3-*TUBG1* (RRID:Addgene\_104433), human *E2F1* sh (RRID:Addgene\_66883) and pcDNA3-*TUBG2* (RRID:Addgene\_171966) were prepared as previously reported.<sup>2,13,14,19,20</sup> The human pSG5L-*RB1* and pcDNA-*E2F1* constructs were kindly provided by Dr. W. Sellers (RRID:Addgene\_10720<sup>21</sup>) and Dr. J.R. Nevins (Duke University, USA<sup>22</sup>), respectively. The human *TUBG1* sgRNA specifically targets a *TUBG1* gene sequence that is not found in *TUBG2*, making *TUBG2* inherently resistant to coexpression with sg*TUBG1*.

The pSpCas(BB)-2A-GFP (PX458) plasmid (a gift from Dr. F. Zhang, MIT; RRID:Addgene\_48138) was prepared as previously described,<sup>23</sup> encoding the sgRNA for human *RB1* with the annealed oligonucleotides, 5'caccgCGGTGGCGGCCGTTTTCGG3' and 5'aaacCCGAAAAACGGCCGCCAC CGc3' (RRID:Addgene\_229857). Human *RB1* (RRID:Addgene\_10720) was prepared using a Quikchange Mutagenesis Kit (Stratagene) and the following oligos (modified bases underlined): 5'C AAAACCCCCCGAAAGACCGCGGCCACCGCCGCC3' and 5'GGCGGCGGT GGCCGCGGTCTTTCGGGGGGTTTG3' (RRID:Addgene\_229856). The flag-tag was inserted in the pcDNA3-*TUBG2* (RRID:Addgene\_171966) vector<sup>20</sup> using a Quikchange Mutagenesis Kit (Stratagene) with the following oligos (inserted bases underlined): 5'TGGAATC ACCATG GATTACAAGGATGACGACGATAAGATCC CCCGGGAGATCAT3' and 5'ATGATCTCCCGGGGATCT TATCGTCGTCATCCTTGTA ATCCATGGTGAATTCCA3' (RRID:Addgene\_229855). The insertions and constructs were verified by sequencing.

## 2.2 | Cell culture and establishing stable transfections

Y79 (ATCC-HTB-18<sup>TM</sup>, RRID:CVCL\_1893), MCF10A (ATCC-CRL-10317<sup>TM</sup>, RRID:CVCL\_0598), A549 (ATCC-CCL-185<sup>TM</sup>, RRID:CVCL\_0023) and U2OS (ATCC-HTB-96<sup>TM</sup>, RRID:CVCL\_0042) cells were cultured according to the instructions provided by the cell distributors. U1690s (RRID:CVCL\_D055), a gift from Dr. J. Bergh,<sup>24</sup>

were cultured at 37°C and 5% CO<sub>2</sub> in RPMI-1640 medium (GE Healthcare HyClone) supplemented with 10% fetal calf serum (Biological Industries), 100 U/mL penicillin, and 100 µg/mL streptomycin (GE Healthcare HyClone). Human H9-NSCs, derived from embryonic stem cells and provided by Dr. L. Karayan-Tapon,<sup>25</sup> were cultured at 37°C and 5% CO<sub>2</sub> in knock-out DMEM/F-12 medium supplemented with 2% Stempro neural supplement, 20 ng/mL recombinant basic fibroblast growth factor, 20 ng/mL recombinant epidermal growth factor (Gibco<sup>TM</sup>), 2 mM Glutamax, 100 U/mL penicillin, and 100 µg/mL streptomycin. Cells were cultured on Geltrex-coated culture dishes (Gibco<sup>TM</sup>) following the manufacturer's instructions. Passaging of cells was performed using StemPro Accutase solution (Gibco<sup>TM</sup>). Neuronally differentiated H9-NSCs were obtained by culturing H9-NSCs for 14 days in neural induction medium (1:1 DMEM-F12 and Neurobasal<sup>TM</sup>-A from Gibco<sup>TM</sup> and Thermo Fisher, respectively) supplemented with serum-free B27 supplement, 2 mM Glutamax, 100 U/mL penicillin, and 100 µg/mL streptomycin. Changes in cell morphology were analyzed by microscopy to assay neuronal differentiation. Cells were treated with either DMSO, 50 nM L12, or vincristine for 24 h before being fixed and immunofluorescently labeled. Stably transfected A549, MCF10A, and U2OS cells were obtained as described elsewhere.<sup>13,16,19</sup> A549 stably expressing *RB1* sgRNA were obtained by isolating Cas9-GFP expressing clones, and the absence of *RB1* expression was confirmed by Western blot analysis. The selected clone was then cotransfected with an sgRNA-resistant *RB1* gene (RRID:Addgene\_10720), and coexpressing clones were obtained by isolation of Cas9-GFP expressing clones and tested the restored *RB1* expression using an anti-*RB1* antibody in Western blot analysis. Stably transfected *TUBG* shRNA-expressing MCF10A cells and *TUBG* shRNA MCF10A cells coexpressing a sh-resistant *TUBG1* gene were obtained by selection with 100 µg/mL zeocin (Fisher Scientific GTF Aktiebolag) or 100 µg/mL zeocin and 200 µg/mL G418 (Promega Biotech AB), respectively. U2OS stably coexpressing *TUBG1* sgRNA and either sgRNA-resistant *TUBG1* or *TUBG2* were obtained by selection with 200 µg/mL G418 combined with the isolation of Cas9-GFP expressing clones. U2OS cells stably expressing pcDNA3-flag-*TUBG2* were obtained by selection with 200 µg/mL G418, and the expression was confirmed by Western blot analysis using anti-TUBG antibodies. We regularly screened all cell lines for the presence of mycoplasma.

## 2.3 | Transfection, and western blot analysis

Transfection was performed using Xfect Transfection Reagent (Takara Bio Europe) following the manufacturer's

instructions. U2OS cells were transfected twice with *E2F1* shRNA or a combination of *E2F1* sgRNA and pcDNA-*E2F1* (1:1 ratio), with a one-day interval between transfections. The cells were analyzed on the fifth day following the first transfection. Biochemical fractions and total lysates of cells were prepared and analyzed by western blotting as described.<sup>13,16,19,20,26</sup> In brief, fractionated cells were lysed in buffer containing 0.1% Triton X-100, and the supernatant constituted the cytosolic fraction. The remaining pelleted nuclei were resuspended in non-salt buffer (3 mM ethylenediaminetetraacetic acid tetrasodium salt dihydrate (EDTA; Scharlau), and 0.2 mM Ethyleneglycol-bis(β-aminoethyl)-N,N,N',N'-tetraacetic acid (EGTA; AppliChem) dissolved in deionized water) and solubilized using three sonication cycles of five seconds each. Total lysates were obtained by mixing both fractions together.<sup>27</sup> After adding loading buffer,<sup>28</sup> the purified fractions were heated, and proteins were separated in an acrylamide gel. The proteins were then transferred onto a 0.22 μm nitrocellulose membrane and analyzed by Western blotting using α-tubulin and histone as molecular markers for the cytosolic and nuclear fractions, respectively.

## 2.4 | Compound selection and large-scale screening

The Chemical Biology Consortium Sweden (CBCS; [www.cbcs.se](http://www.cbcs.se)) provided the initial 11 769 compounds. The compound set consisted of the following libraries: the primary screening set (6040 diverse compounds spanning from drug- to lead-like in terms of molecular size (Mw)), a subset of kinase-directed compounds (1400 compounds), a set of known pharmacologically active compounds and FDA-approved drugs (1200 Prestwick Chemicals; [www.prestwickchemical.com](http://www.prestwickchemical.com)), a set of natural product-derived compounds (3000 compounds from TimTec; [www.timtec.net](http://www.timtec.net)), and 129 mixtures isolated from Cyanobacteria (from Prof. W. Gerwick laboratories; Skaggs school of Pharmacy and Pharmaceutical Sciences). All compounds were dissolved in dimethyl sulfoxide and assessed once at a 10 μM concentration. U2OS cells were batch transfected with 170 ng of the pGL3-TATA-6xEGF-Luc construct,<sup>29</sup> 1 ng of the PRL-CMV-Renilla luciferase reporter construct (Promega Biotech AB) and 10 ng of the pcDNA3-hemagglutinating (HA)hE2F1 construct<sup>22</sup> per 1 × 10<sup>6</sup> cells. Eight hours after transfection, cells were treated with the test compound for 16 h and subsequently lysed in the plate. Double determination of luciferase and *Renilla* activity was achieved using a dual-luciferase reporter assay system (Promega Biotech AB<sup>14,16</sup>). We identified the positive control, 3-(5-methyl-2-(2-oxo-1,2-dihydroindol-3-ylidenemethyl)-1H-pyrrol-3-yl) propionic acid (SU10944), as a compound that increased

the basal activity in a dual-luciferase reporter assay during an initial preliminary screening.

## 2.5 | Synthesis of L12 (4-(6-((3-Methoxyphenyl)amino)pyrimidin-4-yl)-N,N-dimethylbenzenamine)

4-(6-chloropyrimidin-4-yl)-N,N-dimethylbenzenamine: *Notes: a fresh commercial batch of 4-dimethylaminophenylboronic acid (should be white, not dark gray) and a fresh commercial batch of [1,1'-Bis(diphenylphosphino)ferrocene] dichloropalladium(II), complexed with dichloromethane (both from Sigma-Aldrich) were used. Nitrogen gas was bubbled through dry tetrahydrofuran (THF) and 1 M Na<sub>2</sub>CO<sub>3</sub> aqueous solution for 15 min before use.*

4-dimethylaminophenylboronic acid (600 mg, 3.64 mmol) and 4,6-dichloropyrimidine (813 mg, 5.46 mmol) were added to a 10–20 mL microvial, and THF was added under nitrogen using a septum. [1,1'-Bis(diphenylphosphino)ferrocene]dichloropalladium(II) (160 mg, 0.22 mmol) was added, followed by a 1 M aqueous solution of Na<sub>2</sub>CO<sub>3</sub> (7.5 mL). The vial was capped, and nitrogen was bubbled through the mixture for approximately 5 min. The reaction was then heated at 80°C for 16 h. The biphasic reaction mixture was diluted with water (10 mL) and diethyl ether (50 mL); the phases were separated, and the aqueous phase was extracted with diethyl ether (3 × 30 mL). The organic phases were collected and filtered through celite. The residue was purified by column chromatography (SiO<sub>2</sub>, 0%–22% ethyl acetate gradient in *n*-pentane) to obtain the product as a pale yellow crystalline solid (296 mg, 35% yield). <sup>1</sup>H-NMR (CDCl<sub>3</sub>) matches that reported in the literature.<sup>30,31</sup> <sup>1</sup>H NMR (400 MHz, cdcl<sub>3</sub>) δ 8.88 (d, *J* = 1.1 Hz, 1H), 8.00 (d, *J* = 9.1 Hz, 2H), 7.60 (d, *J* = 1.1 Hz, 1H), 6.77 (d, *J* = 9.0 Hz, 2H), 3.07 (s, 6H). <sup>13</sup>C NMR (201 MHz, CDCl<sub>3</sub>) δ 165.5, 161.2, 158.7, 152.6, 128.7, 122.5 (broad), 114.9, 112.1, 40.3.

4-(6-((3-Methoxyphenyl) amino)pyrimidin-4-yl)-N,N-dimethylbenzenamine hydrochloride (L12): To a mixture of 4-(6-chloropyrimidin-4-yl)-N,N-dimethylbenzenamine (230 mg, 0.98 mmol) and 3-methoxyaniline (105 μL, 0.94 mmol) dissolved in tert-butanol (2 mL) in a 2–5 mL microvial to which 4 M HCl in dioxane (62 μL, 2.00 mmol) was added. The vial was capped, and the mixture was heated in a microwave reactor at 110°C for 30 min, leading to the formation of a yellow precipitate. The completion of the reaction was confirmed by thin-layer chromatography (TLC; pentane: ethyl acetate 4:1), indicating full consumption of 3-methoxyaniline. The reaction mixture was kept at 4°C overnight to allow for further precipitation. The resulting precipitate was collected by filtration and washed with a small amount of *t*-butanol and ice-cold diethyl ether (four times), yielding the final product as a yellow



solid (232 mg, 66% yield). HPLC-UV (254 nm): rt. 9.59 min (water: acetonitrile 50:50 to 0:100 with 0.1% trifluoroacetic acid). HRMS (ESI/QTOF)  $m/z$ :  $[M+H]^+$  Calcd for  $C_{19}H_{20}N_4O$  321.1715; Found 321.1714.  $^1H$  NMR (400 MHz,  $dms\text{-}d_6$ )  $\delta$  11.55 (s, 1H), 8.78 (d,  $J=2.3$  Hz, 1H), 7.84 (d,  $J=8.6$  Hz, 2H), 7.40 (s, 2H), 7.36–7.25 (m, 2H), 6.86 (d,  $J=8.6$  Hz, 2H), 6.79 (d,  $J=7.1$  Hz, 1H), 3.77 (s, 3H), 3.03 (s, 6H).  $^{13}C$  NMR (101 MHz,  $dms\text{-}d_6$ )  $\delta$  161.7, 161.6, 160.1, 153.4, 152.9, 152.5, 139.2, 130.3, 128.8, 115.3, 114.4, 112.3, 110.6, 108.2, 55.6, 40.1.

The synthetic scheme for the synthesis of L12 and general information regarding the synthesis and characterization of L12 can be found in [Figure S2](#).

## 2.6 | Analysis of cell cycle and cell death

Cell cycle and cell death analyses were performed as described elsewhere.<sup>3</sup> In brief, after incubation, cells were harvested and fixed in cold 70% ethanol, and cell cycle progression was analyzed in a Nucleocounter® NC-300™ by measuring cell DNA content with diamidino-2-phenylindole (DAPI) as described by the manufacturer (ChemoMetec, Denmark). Cell cycle profiles were analyzed with FlowJo (Tree Star, Inc.).

Cell death was assessed by quantifying the accumulation of hypodiploid cells in the sub-G1 region of the DNA histogram, indicative of apoptotic DNA fragmentation. Additionally, cell death was independently measured using trypan blue staining to evaluate cell membrane integrity and morphology, analyzed with a LUNA automated cell counter (BioNordika).

## 2.7 | Microscopy, $\gamma$ -tubulin and microtubule regrowth assay

U2OS and neuronally differentiated H9-NSC cells were cultured and fixed as described previously.<sup>20,32</sup> The fixation procedure involved a two-step process: first using paraformaldehyde, followed by a final fixation and permeabilization step using a mixture of methanol and acetone (1:1).<sup>32</sup> Confocal fluorescence imaging studies were conducted using a Zeiss LSM 700 Axio Observer microscope equipped with a Plan-Apochromat  $\times 40$  or  $\times 63$  NA 1.40 oil immersion objective. For all images presented in this paper, a rolling ball background subtraction was applied using Fiji. Image analysis, Z-stack projections, and further image processing were performed using the ImageJ (Fiji, [RRID:SCR\\_002285](#)) software.<sup>33</sup>

In the  $\gamma$ -tubule and microtubule regrowth assays, cells were treated and analyzed as described previously.<sup>2,14</sup> For the  $\gamma$ -tubule regrowth assay, cells underwent a 30-min

incubation on ice to depolymerize  $\gamma$ -tubules before fixation. Alternatively, warm medium supplemented with vehicle (DMSO) or L12 was added to the cells to promote  $\gamma$ -tubule polymerization, followed by a 20-min incubation period prior to fixation. The percentage of cells exhibiting  $\gamma$ -tubules was determined based on the counts from each sample.<sup>2</sup> In the microtubule regrowth assay, cells were similarly chilled on ice for 30 min to depolymerize microtubules. Subsequently, these cells were stained either immediately (0 min) or after a 2-min incubation period following the addition of warm medium to promote microtubule polymerization. The warm medium was supplemented with either 2  $\mu$ L/mL DMSO, 10  $\mu$ M colcemid to prevent microtubule polymerization, or in the presence of L12.

## 2.8 | Kinase inhibition profile assay

A radiometric protein kinase assay (33PanQinase® Activity Assay, Biochemical Screening Systems, ProQinase) was utilized to measure the kinase activity of the 397 protein kinases. All kinase assays were conducted in 96-well FlashPlates™ (Perkin Elmer) in a 50  $\mu$ L reaction volume. The reaction cocktail was pipetted in four steps in the following order: 10  $\mu$ L of non-radioactive ATP solution, 25  $\mu$ L of assay buffer/ $[\gamma\text{-}^{33}\text{P}]\text{-ATP}$  mixture, 5  $\mu$ L of test sample in 10% DMSO, and 10  $\mu$ L of enzyme/substrate mixture. The assay for all protein kinases contained 70 mM HEPES-NaOH pH 7.5, 3 mM  $MgCl_2$ , 3 mM  $MnCl_2$ , 3  $\mu$ M Na-orthovanadate, 1.2 mM DTT, ATP (variable amounts, corresponding to the apparent ATP-K<sub>m</sub> of the respective kinase),  $[\gamma\text{-}^{33}\text{P}]\text{-ATP}$  (approx.  $8 \times 10^5$  cpm per well), protein kinase, and substrate. All PKC assays (except the PKC- $\mu$  and the PKC- $\nu$  assay) additionally contained 1 mM  $CaCl_2$ , 4 mM EDTA, 5  $\mu$ g/mL Phosphatidylserine, and 1  $\mu$ g/mL 1,2-Dioleoyl-glycerol. The CAMK1D, CAMK2A, CAMK2B, CAMK2D, CAMK4, CAMKK1, CAMKK2, DAPK2, EEF2K, MYLK, MYLK2, and MYLK3 assays additionally contained 1  $\mu$ g/mL Calmodulin and 0.5 mM  $CaCl_2$ . The PRKG1 and PRKG2 assays additionally contained 1  $\mu$ M cGMP. The DNA-PK assay additionally contained 2.5  $\mu$ g/mL DNA. The protein kinase reaction cocktails were incubated at 30°C for 60 min. The reaction was stopped with 50  $\mu$ L of 2% (v/v)  $H_3PO_4$ , and plates were aspirated and washed two times with 200  $\mu$ L 0.9% (w/v) NaCl. All assays were performed with a BeckmanCoulter Biomek 2000/SL robotic system. Incorporation of  $^{33}\text{P}$  (counting of “cpm”) was determined with a microplate scintillation counter (Microbeta, Wallac). In the lipid kinase assays, the non-radiometric ADP-Glo™ Assay (Promega Biotech AB) was used to measure the activity of the 13 lipid kinases. All kinase assays were performed in 96-well half-area microtiter plates from Greiner Bio-One (Frickenhausen, Germany) in a 25  $\mu$ L reaction volume. The reaction cocktail was pipetted

in three steps in the following order: 10  $\mu$ L of ATP solution, 5  $\mu$ L of test sample in 10% DMSO, and 10  $\mu$ L of enzyme/substrate mixture. All lipid kinase assays contained 50 mM HEPES-NaOH, pH 7.5, 1 mM EGTA, 100 mM NaCl, 0.03% CHAPS, 2 mM DTT, ATP (variable amounts, corresponding to the apparent ATP- $K_m$  of the respective kinase), kinase, and substrate. The assay for PI4KB, PIK3C3, PIK3C2B, and PI4K2A additionally contained 3 mM  $MnCl_2$ , while the assay for PIK3C2A, PIK3C2G, PIK3CA/PIK3R1, PIK3CB/PIK3R1, PIK3CD/PIK3R1, and PIK3CG additionally contained 3 mM  $MgCl_2$ . The lipid kinase reaction cocktails were incubated at 30°C for 40 min. The reaction was stopped with 25  $\mu$ L ADP-Glo reagent per well. Plates were incubated for 40 min at room temperature, followed by the addition of 50  $\mu$ L kinase detection reagent per well and incubation for a further 60 min at room temperature. Signals were measured with a microplate multilabel reader (Victor2, Perkin Elmer) in luminescence mode.

All protein kinases were expressed in Sf9 insect cells or in *E. coli* as recombinant GST-fusion proteins or His-tagged proteins, either as full-length or enzymatically active fragments. All kinases were produced from human cDNAs and purified by either GSH affinity chromatography or immobilized metal affinity chromatography. Affinity tags were removed from kinases during purification. The purity of the protein kinases was examined by SDS-PAGE/Coomassie staining, and the identity was checked by mass spectrometry.

## 2.9 | Cellular thermal shift assay

To demonstrate that L12 directly binds to TUBG1, we monitored the effect of L12 on the thermodynamic stabilization of TUBG upon ligand binding, as previously described.<sup>3,34</sup> Briefly, cells were harvested and resuspended ( $2 \times 10^6$  cells/mL) in phosphate saline buffer (PBS) supplemented with protease inhibitors. The suspension was then heat-treated as described.<sup>34</sup> Alternatively, cells treated with L12 or vehicle (DMSO) were incubated for 30 min at 4°C on a tube rotator before being resuspended in PBS. Cell lysates were prepared by subjecting the cells to three freeze-thaw cycles. The resulting cell lysates were analyzed by Western blotting.

## 2.10 | Structural analysis and molecular docking of human TUBG1

The crystal structure of human TUBG1 bound to a non-hydrolysable GTP analogue was sourced from the Protein Data Bank (PDB file: 1Z5V<sup>35</sup>) for initial structural analysis. Given that this X-ray structure lacked six short loops, 3D models of the complete protein were generated with

Alpha-Fold (AF) and Swiss-Model.<sup>36,37</sup> To assess the protein's flexibility, we employed ExProSe (Exploration of Protein Structure),<sup>38</sup> implemented in Julia—a programming language chosen for its readability and computational efficiency. This distance geometry-based approach facilitated the creation of an ensemble of protein structures from an initial 3D model, allowing for investigations of potential allosteric mechanisms and cryptic ligand binding pockets.

In the present study, we generated 20 distinct conformations based on the Swiss-Model's predicted 3D structure of human TUBG. These structures were then clustered (10 families of conformation were considered based on RMSD measurements), and a representative model with an open colchicine pocket—differing from the X-ray, AF-model, and Swiss-Model 3D structures—was selected for in-depth analysis. The X-ray structure of  $\alpha$ -tubulin and  $\beta$ -tubulin complexed with nocodazole (PDB file 7Z2P) served as a reference for evaluating the human TUBG simulated 3D models using ExProSe.<sup>39,40</sup>

Putative ligand binding pockets within the TUBG structure were predicted with the Python package pyKVFinder<sup>41</sup> (RRID:SCR\_006903). Further, the physicochemical attributes of the L12 compound, along with structural alerts following Eli Lilly's demerit filtering method, were examined using FAF-Drugs.<sup>42,43</sup> Lastly, molecular docking studies were conducted using the Smina software,<sup>44</sup> incorporating various scoring functions such as Vina,<sup>45</sup> Vinardo,<sup>46</sup> and a recalibrated Vina scoring function.<sup>47</sup>

## 2.11 | Xenograft tumor treatment

Xenograft tumors derived from the human small cell lung carcinoma U1690 cell line were established as previously described.<sup>16</sup> In brief, six- to eight-week-old female athymic mice (NMRI strain nu/nu; Charles River, Sulzfeld, Germany) were subcutaneously injected in the left flank with  $10^7$  cells suspended in Matrigel basement membrane matrix (Corning) according to the manufacturer's instructions. Treatment was initiated once tumors reached an average size of 105 mm<sup>3</sup>, with animals bearing tumors smaller or larger than this threshold excluded from the study. The mice were randomized into treatment groups of 8 animals each, based on tumor volumes calculated using the formula:  $(width \times length)^2/2$ . Mice received intraperitoneal injections three times per week with either Miglyol Oil 812 (Cremer Oleo GmbH & Co. KG) as a vehicle control or L12 dissolved in Miglyol Oil 812. Tumor growth and body weight were monitored throughout the study. Upon tumors reaching a volume size of 1 cm<sup>3</sup>, mice were euthanized, and the tumors were

excised and weighed. Based on this endpoint, the attrition rate was 37.5% in the control group and 12.5% in the treatment group.

For this initial study, we chose female mice to minimize biological variability and enhance experimental consistency. Female athymic mice exhibit fewer androgen-related hormonal fluctuations that could potentially influence tumor growth or drug response, even in non-hormone-dependent cancer models.<sup>48</sup> Additionally, female mice are less prone to aggression and stress when housed together, which reduces confounding variables that could affect tumor growth or general health during the study.<sup>49</sup> Future studies will include male mice to evaluate potential sex-specific differences in drug efficacy and tumor biology.

All animal experiments were conducted in accordance with the guidelines approved by the regional ethical committee for animal research (LaGeSo Berlin, Germany, approval no. A0452/08). The experiments were performed by Experimental Pharmacology & Oncology Berlin-BUCH (EPO-GmbH, Germany).

## 2.12 | Statistics

All data are expressed as means  $\pm$  standard deviation, and the statistical significance of differences between two or more groups was analyzed by paired Student's *t* test or by two-way ANOVA (\**p* < .05, \*\**p* < .01, \*\*\**p* < .001, \*\*\*\**p* < .0001) using Prism 6 software (RRID:SCR\_005375). Cell cycle profiles were assessed using FlowJo (Tree Star, Inc., RRID:SCR\_008520).

## 3 | RESULTS

### 3.1 | Compounds influencing E2F activities in a luciferase assay

Mutations, deletions, and hyperphosphorylation-induced inactivation of RB1 serve as crucial triggers for initiating E2F transcriptional activity, leading to uncontrolled cell divisions. These aberrations are commonly implicated in various diseases, including retinoblastoma, osteosarcoma, neuroblastoma, prostate cancer, colorectal cancer, small cell lung cancer, breast cancer, and lymphoblastic leukemia, all of which often exhibit defects in the RB1 signaling pathway.<sup>15,50–52</sup>

Building upon the evidence that TUBG modulates E2Fs activities by acting as a co-regulator of transcription,<sup>14,53</sup> and the finding that SadB-mediated phosphorylation of TUBG on Ser<sup>385</sup> promotes its nuclear localization and subsequent interaction with E2F

transcription factors,<sup>14,54</sup> we sought to investigate potential therapeutic implications of targeting this pathway. The nuclear localization of TUBG is critical for its regulatory activity on E2Fs, which are central to cell cycle control and tumor progression.<sup>9,14,20</sup> Recognizing the imperative for novel therapies with reduced side effects, we conducted a high-throughput screening of selected compounds designed to target SadB or nuclear TUBG activities. For this purpose, human osteosarcoma cells (U2OS), transiently expressing luciferase reporter plasmids containing E2F-binding sites, were exposed to 11 769 compounds to evaluate their impact on E2F transcriptional activity (Figures S1A and S1B).<sup>29,54</sup>

Using a 50% increase in activity as a threshold, we identified 51 compounds that enhanced the baseline luciferase activity due to the endogenous activity of E2F (Figure S1B). Subsequent hit confirmation analysis identified only five compounds that exhibited a concentration-dependent increase in baseline luciferase activity (Figure S1C).

Next, we screened 96 analogues derived from the initial five identified hits, assessing their ability to induce cell death in various cell lines with RB1 signaling pathway defects.<sup>13</sup> Among these analogues, we identified L12 as the most promising (Figure 1A). L12 is a drug-like small molecule (e.g., MW = 320; logP = 3.8) identified in a kinase inhibitor library that complies with the toxicophore structural criteria established by Eli Lillys (according to the regular filtering mode).<sup>43</sup>

### 3.2 | L12 demonstrates cytotoxicity towards cells with an impaired RB1 signaling pathway

To validate the cytotoxic mechanism of L12 and address the concern regarding the reliance on sub-G1 values obtained from cell cycle analysis, we performed complementary trypan blue staining. This approach confirmed that the sub-G1 populations observed in the cell cycle profiles correspond to dead cells, providing additional confidence in the cytotoxic effect of L12 (Figure S1D).

Comparative analysis revealed that, when compared to non-cancerous cells with a functional RB1 pathway (human mammary gland epithelial MCF10A cells; Figure 1B), L12 exhibited heightened toxicity in cells lacking RB1 expression (human retinoblastoma Y79, small cell lung carcinoma U1690 cells; Figure 1B), as well as in cells with a constitutively phosphorylated RB1 (human osteosarcoma U2OS cells lacking expression of *p16<sup>INK</sup>*,<sup>55</sup> leading to constitutive phosphorylation of RB1; Figure 1B), with an IC<sub>50</sub> value for the cytotoxic effect of L12 at 30.13 nM (Figures 1B and S1E). It is worth noting

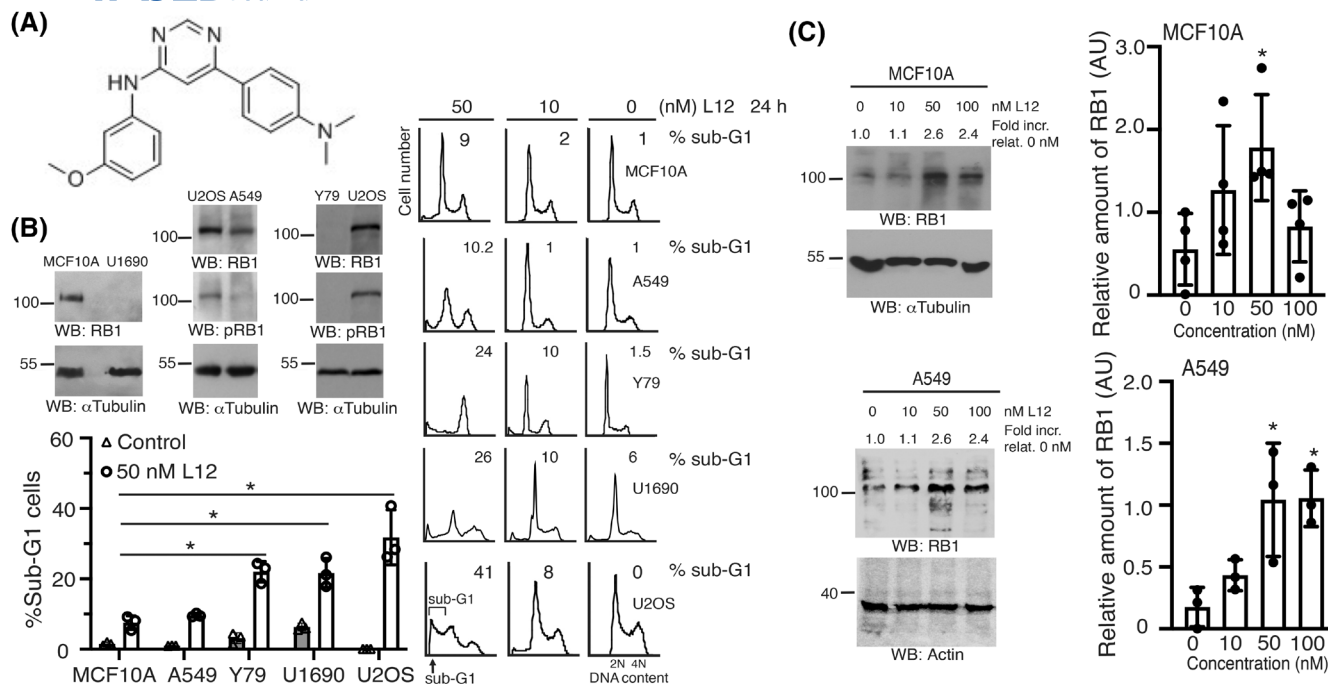


**FIGURE 1** Cytotoxic effect of L12 treatment and its dependency on the RB1 pathway functionality. (A) Depiction of the structure of L12. (B) Western blotting (WB) analysis of RB1 and phosphorylated Ser<sup>780</sup> RB1 proteins using an anti-RB1 (RB1) and anti-phospho-Ser<sup>780</sup> RB1 (pRB1) antibodies. Total lysates from various cell lines were probed, including the RB1-deficient human retinoblastoma Y79, the osteosarcoma U2OS with a constitutively phosphorylated RB1 at Ser<sup>780</sup> (pRB1), the mammary gland epithelial cell line MCF10A, and the adenocarcinoma alveolar basal epithelial A549, both with functional RB1 pathways, as well as the RB1-deficient small cell lung carcinoma U1690.  $\alpha$ -tubulin ( $\alpha$ Tubulin) served as a loading control. Cells treated with different L12 concentrations for 24h were assessed for cell accumulation in the sub-G1 fraction (indicating dead cells). The histograms depict mean  $\pm$  SD of the percentages of cells in the sub-G1 fractions ( $N=3$ ;  $*p < .05$ ). (C) Examination of L12's impact on the downstream gene target of TUBG, *RB1*, was conducted by WB analysis using an anti-RB1 antibody on MCF10A and A549 cell lysates.  $\alpha$ -tubulin and actin were utilized as loading controls. Numbers on the western blot indicate variations in RB1 expression compared to the vehicle control. To account for protein loading discrepancies, RB1's protein concentration was normalized to its ratio with the respective loading control for each treatment. The graph displays relative RB1 protein expression across MCF10A ( $N=4$ ) and A549 ( $N=3$ ) cell lines when treated with varying L12 concentrations, with data presented as mean  $\pm$  SD. Please note that the intensity of the RB1 bands may vary between figures as a result of adjusted exposure times for western blot analysis. These adjustments were made to prevent overexposure and to accurately capture differences in RB1 expression levels across experimental conditions.

that in Y79 cell populations, in the absence of expression of RB1, L12 treatment also induced a significant accumulation of cells in G2 (Figure 1B).

To further investigate the selectivity of L12, the cell cycle profile of adenocarcinoma alveolar basal epithelial cell line A549 (which expresses RB1 protein) was compared to that of MCF10A cells. L12 treatment has a more profound effect on A549 cells compared to MCF10A cells (Figure 1B). While RB1 is expressed in both cell lines, the observed cytotoxic effect of L12 on A549 cells may be attributed to the presence of a KRAS mutation in A549. This mutation drives growth factor-independent proliferation and may bypass RB1 pathway regulation in controlling cell division.<sup>56</sup> Moreover, prior findings have demonstrated that nuclear TUBG activity is essential for the recruitment of PCNA to the origin of replication.<sup>20</sup> It can be speculated that the increased proliferative rate observed

in cells harboring oncogenic mutations such as KRAS necessitates active nuclear TUBG, a function potentially disrupted by L12. Together, these factors may contribute to the selective cytotoxic effects of L12.

These findings support the hypothesis that L12 selectively targets cancer cells with an impaired RB1 pathway or associated mechanisms.

### 3.3 | The in vitro impact of L12 as a kinase inhibitor

Since the structure of L12 classifies it as a potential kinase inhibitor, we investigated the kinases that L12 might inhibit through a kinase inhibition profile assay. After treatment of 410 kinase assays (397 protein kinase assays and 13 lipid kinase assays) with L12, three kinases



(KITD816V, Mitogen-Activated Protein Kinase Kinase Kinase Kinase 5 [MAP4K5], and MAPK Activated Protein Kinase 2 [MAPKAPK2]) in the tested panel were affected after treatment with 3  $\mu$ M L12 (Supplementary Table S1), which is 100-fold higher than the determined IC<sub>50</sub> concentration (IC<sub>50</sub> = 30.13 nM; Figures 1B and S1E). These data imply that the cytotoxic effects of L12 on the TUBG–RB1 network most likely do not depend on the inhibition of kinases.<sup>57–59</sup> These data strongly suggest that L12's cytotoxic effect on cell lines depends on the inhibition of another cellular target.

### 3.4 | Changes in the protein levels of the TUBG–E2F1–RB1 network alter the toxicity of L12

The inverse correlation between TUBG and RB1 protein expression<sup>13,14</sup> suggests that inhibition of the nuclear activity of TUBG should increase the protein levels of RB1. Additionally, in cells with a defective RB1 pathway, inhibition of TUBG1 activities is expected to result in an E2F1-dependent upregulation of apoptotic genes, such as procaspase 3.<sup>13,14,60</sup> To test the effect of L12 on the expression of RB1, MCF10A and A549 cell populations were treated with various concentrations of L12 and analyzed by western blotting (Figure 1C). L12 treatment increased the protein levels of RB1 in both cell lines (Figure 1C), supporting the idea that L12 targets the activities of TUBG.

To further investigate this hypothesis, we reduced the expression of TUBG by stably expressing short hairpin (sh)RNA-*TUBG* vector (reducing the expression of TUBG protein levels<sup>13,14</sup>) in MCF10A cells (MCF10A-shRNA-*TUBG*). In comparison with MCF10A cells, reduced expression of TUBG protein increased both the cytotoxic effects of L12 (Figure 2A) and the expression levels of RB1 (Figure 2B).<sup>13</sup> However, this increase in RB1 did not provide protection against L12-induced toxicity, suggesting that the cytotoxic effects of L12 are mediated by an additional mechanism beyond RB1 restoration. Moreover, stable expression of a sh-resistant *TUBG1* gene in MCF10A-shRNA-*TUBG* cells reversed both the increased sensitivity to L12 and the RB1 upregulation (Figure 2A,B). These findings suggest that L12 may act as an inhibitor of the nuclear activity of TUBG, with its cytotoxic effects being influenced by RB1 signaling dynamics.

To determine if the cytotoxic effect of L12 is mediated by E2F1-mediated expression of procaspase 3, we transiently reduced E2F1 expression in U2OS cells using shRNA and treated the cells with 50 nM L12 (Figure 2C,D). In cells with reduced E2F1 expression, both the cytotoxicity of L12 and the levels of procaspase 3 were attenuated compared to control U2OS cells or U2OS cells co-expressing

shRNA-*E2F1* and E2F1 (Figure 2C,D). These findings demonstrate that the E2F1-mediated procaspase 3 expression is crucial for the cytotoxic effects of L12.<sup>13</sup>

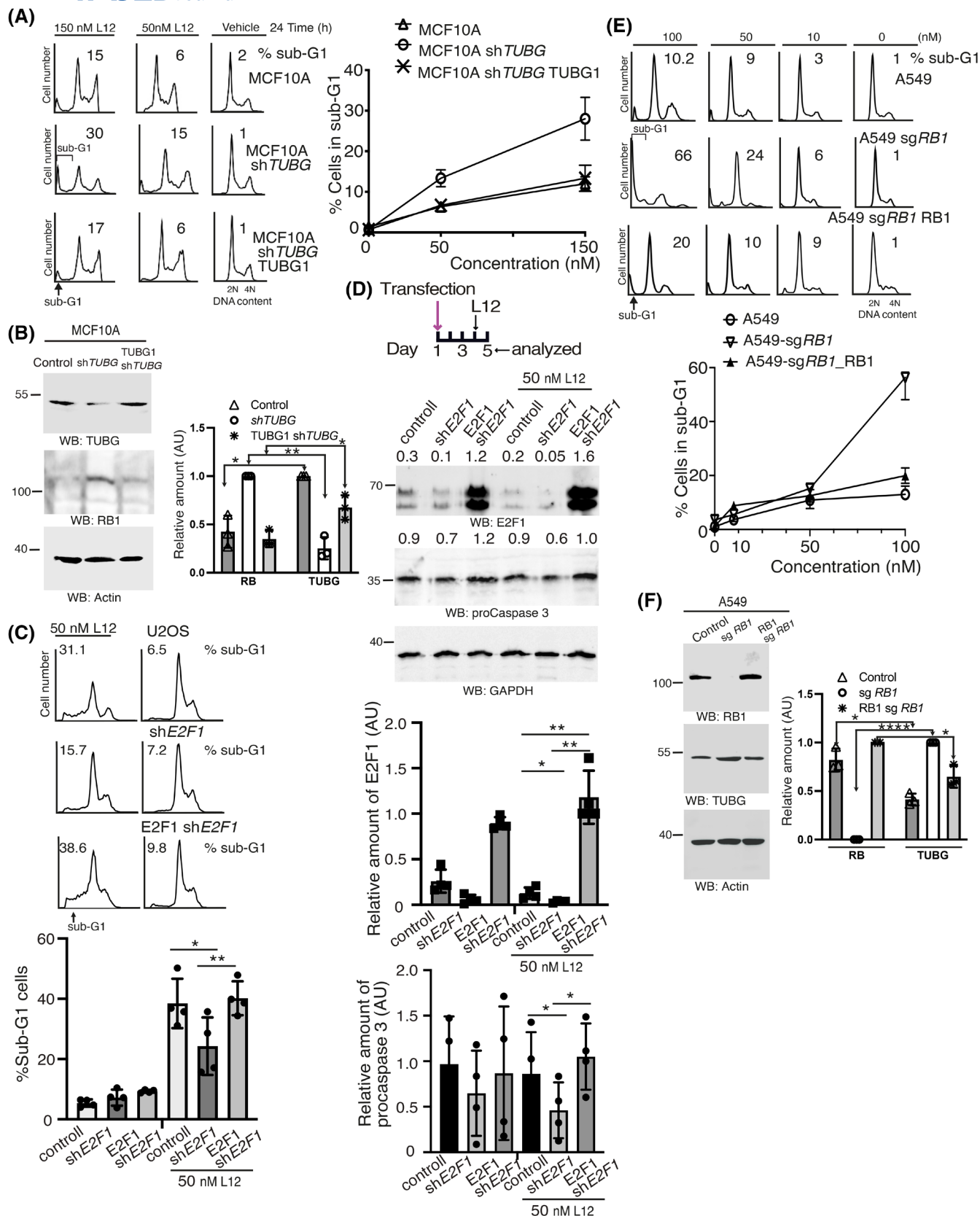
To further ascertain that L12 targets the TUBG–RB1 network, we sought to investigate the effect of knocking down the expression of RB1 by the stable expression of single guide (sg)RNA-*RB1* in A549 cells (A549-sgRNA-*RB1*; Figure 2E,F). In the absence of RB1 expression, the cytotoxic effect of L12 treatment was accentuated (Figure 2E), along with increased protein levels of TUBG (Figure 2F), and expression of a sg-resistant *RB1* gene reverted the observed effects (Figure 2E,F). Altogether, these data prove that L12 interferes with the activities of the TUBG–E2F1–RB1 network.

### 3.5 | L12 toxicity is increased in cells expressing TUBG1

Human *TUBG1* is the most ubiquitous and predominantly expressed gene, while *TUBG2* is expressed during embryonic development and in the brain.<sup>8</sup> *TUBG1* (NP001061.2) and *TUBG2* (BC009670.2) proteins exhibit an amino acid level identity of 97.55%.<sup>11,14</sup> These differences result in a size shift in SDS gels, and in different antibodies being able to distinguish between the two isoforms.<sup>20</sup>

To evaluate the impact of L12 on TUBG1 and TUBG2, we treated human U2OS cells stably expressing *TUBG1*-sgRNA (resulting in the knockout of the *TUBG1* gene; *TUBG1*-sgRNA-U2OS; Figure S3) and co-expressing either a sg-resistant *TUBG1* (*TUBG1*-sgRNA-U2OS-*TUBG1*) or *TUBG2* (*TUBG1*-sgRNA-U2OS-*TUBG2*; Figure 3A<sup>3</sup>). We then examined the effect of L12 on cell division. Nuclear counter analysis showed that L12-treated *TUBG1*-sgRNA-U2OS-*TUBG1* cells died in a dose-dependent manner, but the cytotoxic effect of L12 treatment was attenuated in *TUBG1*-sgRNA-U2OS-*TUBG2* (Figure 3A), suggesting that the binding of L12 to TUBG1 and TUBG2 differs. It is noteworthy that the expression of *TUBG1*-sgRNA in U2OS cells is lethal, indicating that U2OS only expresses TUBG1. Additionally, the specific sequence encoded in *TUBG1*-sgRNA is absent in *TUBG2*.

Since nine of the eleven amino acids that differentiate TUBG1 from TUBG2 are located in the DNA binding domain at the C-terminus (Figure 3A), we investigated the cellular distribution of TUBG1 and TUBG2 in the following cell lines: U2OS, *TUBG1*-sgRNA-U2OS-*TUBG1*, *TUBG1*-sgRNA-U2OS-*TUBG2*, and U2OS that stably express an N-terminal Flag-tagged *TUBG2* gene (U2OS-Flag-*TUBG2*; Figure 3B). Analysis of biochemical fractionations revealed that the largest pool of chromatin-associated TUBG was found in the chromatin fractions prepared from *TUBG1*-sgRNA-U2OS-*TUBG1* cells. Furthermore,



the expression of TUBG2 in U2OS cells diminished the pool of chromatin-associated TUBG. Notably, compared to *TUBG1*-sgRNA-U2OS-TUBG1 cells, *TUBG1*-sgRNA-U2OS-TUBG2 cells exhibited increased expression of RB1

(Figure 3C). Interestingly, both *TUBG1*-sgRNA-U2OS-TUBG1 and *TUBG1*-sgRNA-U2OS-TUBG2 cells exhibited higher expression levels of either TUBG1 or TUBG2 compared to control U2OS cells (Figure 3C). However, the

**FIGURE 2** Influence of TUBG1, E2F1, and RB1 protein levels on the cytotoxic effect of L12 treatment. (A and B) The MCF10A cell lines used include: Control (MCF10A, non-modified parental cells), MCF10A sh *TUBG* (stably expressing *TUBG* shRNA) and MCF10A sh *TUBG* TUBG1 (stably co-expressing *TUBG* shRNA and a sh-resistant *TUBG1* gene). (A) MCF10A cells were treated with DMSO (vehicle) or the indicated concentrations of L12 for 24 h. DNA content was measured by nuclear counter to determine the cell cycle profile and the percentage of cells in the sub-G1 fraction (indicative of dead cells). Histograms display the results, and graphs summarize the mean  $\pm$  SD percentages of sub-G1 cells ( $N=3$ ; two-way ANOVA, \*\*\*\* $p < .0001$ ). (B) Western blotting (WB) was performed to analyze TUBG and RB1 protein levels in total lysates using anti-TUBG and anti-RB1 antibodies. Actin served as the loading control. Graphs illustrate relative protein expression (Student's *t* test,  $N=3$ , \* $p < .05$ , \*\* $p < .01$ ). (C and D) The U2OS cell lines used include: Control (U2OS, non-modified parental cells), U2OS sh *E2F1* (transiently expressing *E2F1* shRNA) and U2OS *E2F1* sh *E2F1* (transiently co-expressing *E2F1* sgRNA and a *E2F1* gene). U2OS cells were treated with DMSO (vehicle) or 50 nM L12 for 24 h. (C) DNA content was measured to determine the cell cycle profile and the percentage of cells in the sub-G1 fraction. Histograms show representative data, and graphs summarize the mean  $\pm$  SD percentages of sub-G1 cells ( $N=4$ ; Student's *t* test, \* $p < .01$ , \*\* $p < .01$ ). (D) WB was used to analyze E2F1 and procaspase 3 protein levels in total lysates using anti-E2F1 and anti-procaspase 3 antibodies. GAPDH served as the loading control. Graphs display relative protein expression (Student's *t* test,  $N=4$ , \* $p < .05$ , \*\* $p < .01$ ). The numbers above the blots (WB) represent the normalized intensity of the protein bands. (E and F) The A549 cell lines used include: Control (A549, non-modified parental cells), A549 sg *RB1* (stably expressing *RB1* sgRNA) and A549 *RB1* sgRNA *RB1* (stably co-expressing *RB1* sgRNA and a sg-resistant *RB1* gene). (E) A549 cells were treated with DMSO (vehicle) or the indicated concentrations of L12 for 24 h. The cell cycle profile and percentage of sub-G1 cells were determined. Histograms represent the results, and graphs show mean  $\pm$  SD percentages of sub-G1 cells ( $N=3$ ; two-way ANOVA, \*\*\*\* $p < .0001$ ). (F) WB analyzed TUBG and RB1 protein levels in total lysates using anti-TUBG and anti-RB1 antibodies. Actin served as the loading control. Graphs depict relative protein expression (Student's *t* test,  $N=3$ , \* $p < .05$ , \*\*\*\* $p < .0001$ ). To ensure accurate comparisons of RB1 protein levels under different conditions, Western blot exposure times were optimized for each experiment to balance signal detection and prevent overexposure, enabling the detection of subtle differences in RB1 expression.

only cell line with reduced RB1 levels was the one with increased TUBG1 expression, i.e., *TUBG1*-sgRNA-U2OS-TUBG1 cells (Figure 3C). This observation may provide a mechanistic explanation for the reduced RB1 levels in *TUBG1*-sgRNA-U2OS-TUBG1 cells, as previous studies have suggested an inverse correlation between TUBG1 and RB1 expression.<sup>13,14,16,17</sup> Altogether, these findings imply that TUBG2 preferentially localizes to the cytoplasm, leading to a reduced pool of chromatin-associated TUBG2, which in turn raises the levels of RB1 expression (Figure 3C).

### 3.6 | The distinct meshwork properties of TUBG1 and TUBG2

Immunofluorescence analysis of fixed U2OS cells stably expressing an N-terminal Flag-tagged *TUBG2* with an anti-Flag antibody revealed that, in the presence of TUBG1 and Flag-TUBG2, the Flag antibody detected limited amounts of TUBG2 at  $\gamma$ -tubules and centrosomes. This suggests that TUBG1 is more prone to forming  $\gamma$ -tubules and localizing to centrosomes (Figure 3D).<sup>2,4,15</sup> In contrast, the largest number of  $\gamma$ -tubules was observed in *TUBG1*-sgRNA-U2OS-TUBG1 cells (Figure 3E). Conversely, *TUBG1*-sgRNA-U2OS-TUBG2 cells rarely formed  $\gamma$ -tubules (Figure 3E), with the cell shown in Figure 3E representing one of the seven cells identified to form  $\gamma$ -tubules in this cell population. These findings indicate that the meshwork properties

of TUBG1 and TUBG2 differ significantly. The low levels of TUBG2 detected in  $\gamma$ -tubules and centrosomes in cells co-expressing TUBG1 and TUBG2, coupled with the limited number of cells expressing only TUBG2 that form  $\gamma$ -tubules in *TUBG1*-sgRNA-U2OS-TUBG2 cell populations, suggest that TUBG1 and TUBG2 exhibit distinct biological traits. These differences may underlie the variable responses observed upon L12 treatment in *TUBG1*-sgRNA-U2OS-TUBG1 and *TUBG1*-sgRNA-U2OS-TUBG2 cells.

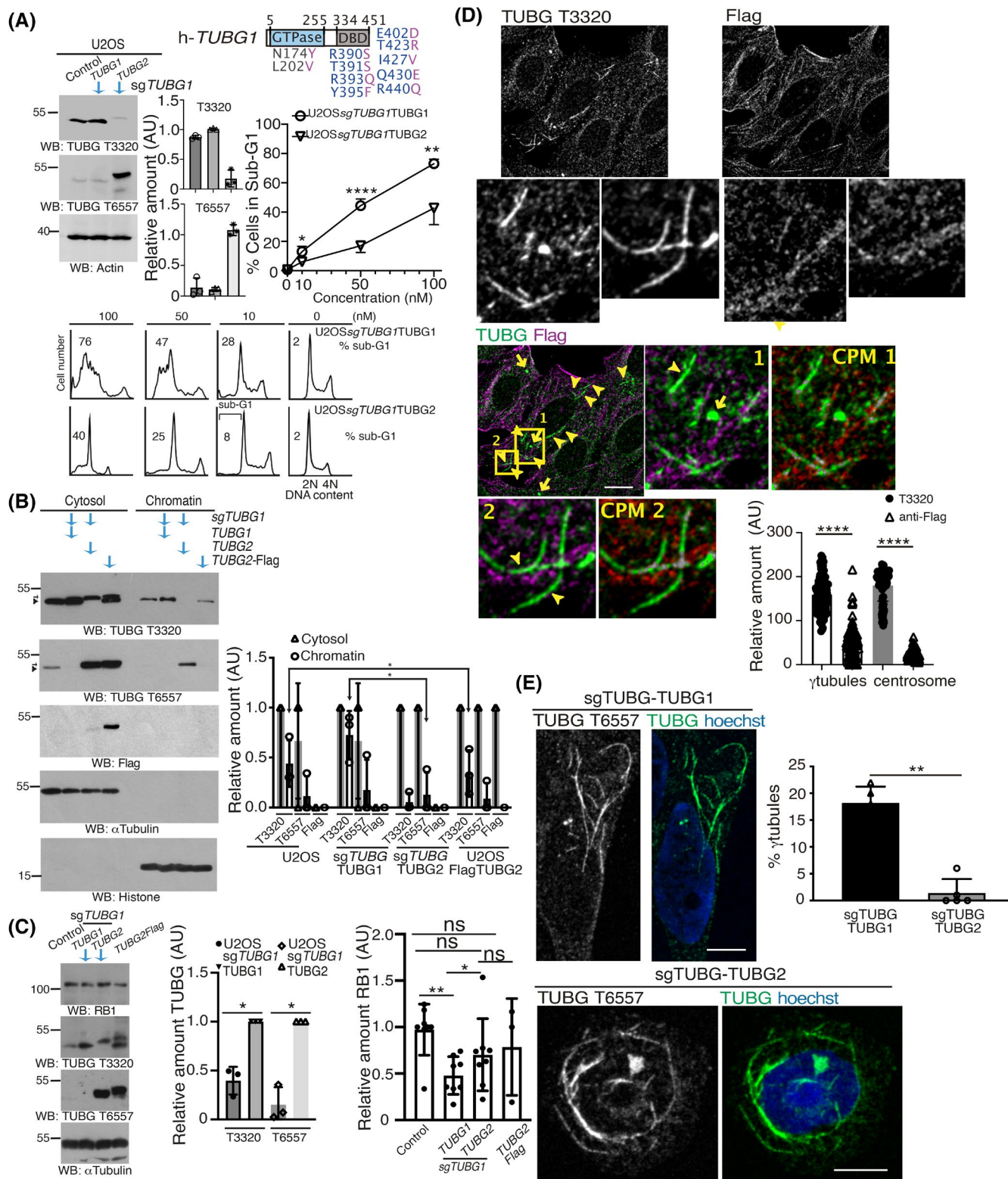
### 3.7 | L12 is a $\gamma$ -tubule polymerizing agent

To assay the effect of L12 on the dynamics of the  $\gamma$ -tubulin meshwork, we investigated the effect of L12 treatment on  $\gamma$ -tubule nucleation by pretreating interphase cells with cold (30 min, depolymerized  $\gamma$ -tubules<sup>2</sup>) and measuring re-growth after placing the cells at 37°C for 20 min (Figure 4A). Immunofluorescence analysis revealed that treatment with L12 increased the number of cells with  $\gamma$ -tubules, suggesting that L12 is a  $\gamma$ -tubule-stabilizing agent.

### 3.8 | Comparative effects of vincristine and L12 treatment on neuronal axons

A potential drawback of microtubule-targeting drugs, such as vincristine, is the occurrence of sensorimotor





neuropathy in children, attributed to axonal damage caused by their action on microtubules.<sup>61</sup> To assess the potential impact of L12 on neuronal axons, we differentiated human H9 neural stem cells into neurons before treating them with either L12 or vincristine. A comparative fluorescence microscopy analysis revealed that

after 24 h of treatment, 50 nM vincristine reduced the intensity of the axon marker  $\beta 3$ -tubulin compared to non-treated or 50 nM L12-treated neurons (Figure 4B). This indicates that L12 treatment demonstrated less neuronal axonal toxicity compared to vincristine treatment.



**FIGURE 3** Variable cytotoxic effects of L12 in cells expressing TUBG1 vs. TUBG2. (A) U2OS cells, U2OS cells stably expressing Flag-tagged *TUBG2* (TUBG2-Flag), or *TUBG1* single guide (sg) RNA (sg*TUBG1*, resulting in TUBG1 knockout) co-expressing either sg-resistant *TUBG1* or a sg-resistant *TUBG2* were treated with DMSO (vehicle) or varying concentrations of L12 for 24 h. Total lysates were analyzed by western blotting (WB;  $N=3$ ). Antibodies targeting the C-terminus (T3320, rabbit) or N-terminus (T6557, mouse) of TUBG were used to detect endogenous and recombinant TUBG proteins, with actin serving as a loading control. DNA content was measured using a nuclear counter, and histograms display cell cycle profile changes, specifically in the sub-G1 fraction. Graphs present normalized TUBG1 and TUBG2 levels (from WB) relative to actin and mean  $\pm$  SD percentages of cells in the sub-G1 fraction ( $N=3$ ). A schematic highlights the GTPase domain (residues 5–255) and DNA-binding domain (DBD; residues 334–451) of the human *TUBG1* (h-*TUBG1*) gene. Amino acid differences between TUBG1 and TUBG2 are shown, with gray and blue indicating TUBG1-specific residues and magenta denoting TUBG2-specific residues. (B) WB analysis of cytosolic (Cytosol) and chromatin fractions from the indicated U2OS cells. Antibodies targeting TUBG's C-terminus (T3320, rabbit) or N-terminus (T6557, mouse) were used to detect endogenous and recombinant TUBG proteins. T3320 preferentially detects TUBG1, while T6557 preferentially detects TUBG2, especially in fractionated samples, where T6557's specificity for TUBG1 improves. Densitometric analysis of TUBG1 and TUBG2 levels are shown, normalized to  $\alpha$ -tubulin (cytosolic marker) or histone (chromatin marker). An anti-flag antibody was used to detect TUBG2-Flag. (C) WB analysis of total lysates shows RB1, TUBG1, and TUBG2 protein levels using anti-RB, T3320, and T6557 antibodies. An  $\alpha$ -tubulin ( $\alpha$ Tubulin) served as a loading control. The graphs depict relative RB1, TUBG1, and TUBG2 expression across the indicated cell lines (RB1: *TUBG1*-sgRNA-U2OS-TUBG1 and *TUBG1*-sgRNA-U2OS-TUBG2,  $N=8$ ; U2OS-TUBG2 Flag,  $N=3$ ; TUBG1: U2OS and *TUBG1*-sgRNA-U2OS-TUBG1,  $N=3$ ; TUBG2: U2OS and *TUBG1*-sgRNA-U2OS-TUBG2,  $N=3$ ). (D) Confocal microscopy images of U2OS-TUBG2-Flag cells stained with an anti-TUBG and anti-Flag antibodies. Images highlight the location of TUBG2-Flag at  $\gamma$ -tubules and centrosomes. Colocalization pixel maps (CPM) of magenta/red and green channels are included. White regions signify colocalization, with arrowheads and arrows indicating  $\gamma$ -tubules and centrosomes, respectively. Scale bars: 10  $\mu$ m. Graphs show the fluorescence intensity of T3320 (TUBG1) or anti-Flag (TUBG2) found at  $\gamma$ -tubules and centrosomes (Student's  $t$  test, \*\*\*\* $p < .0001$ ;  $\gamma$ -tubules:  $N=127$ ; centrosomes:  $N=108$ ). Note that the issue of antibody specificity encountered in WB analysis does not affect immunofluorescence assays, as the proteins maintain a different conformation that is not influenced by SDS treatment. (E) Confocal microscopy images of *TUBG1*-sgRNA-U2OS-TUBG1 and *TUBG1*-sgRNA-U2OS-TUBG2 cells stained with anti-TUBG antibodies. Graphs display the mean percentages of cells with  $\gamma$ -tubules ( $N=5$ ; Student's  $t$  test, \*\* $p < .01$ ) Hoechst was used for nuclear staining. Scale bars: 10  $\mu$ m.

### 3.9 | Characterizing L12 binding to TUBG with CETSA

To investigate the potential direct binding of L12 to TUBG, we employed the Cellular Thermal Shift Assay (CETSA), a biophysical technique that monitors the stabilization of a protein against thermal denaturation upon compound binding.<sup>34</sup> For the initial experiments, we used Y79 cells, which naturally grow in suspension and express TUBG1. Live Y79 cells were exposed to a temperature gradient, and the levels of soluble TUBG were assessed by western blot (Figure 5A). As nearly all of the TUBG pool aggregated at 58°C, this temperature was selected for subsequent testing of L12 (Figure 5B). Treatment of Y79 cells with L12 revealed that L12 thermostabilized TUBG at nanomolar concentrations, indicating a direct interaction between L12 and TUBG (Figure 5B). Additionally, we observed a non-significant trend toward the thermostabilization of  $\alpha$ -tubulin upon L12 treatment, suggesting potential indirect effects of L12 on the microtubule network.

### 3.10 | L12 does not thermostabilize TUBG2

To further evaluate the specificity of L12 binding to TUBG isoforms, we investigated the effect of L12 on TUBG2 using

genetically engineered U2OS cells. Unlike Y79, which predominantly expresses TUBG1, the *TUBG1*-sgRNA-U2OS-TUBG2 cells used here were modified to lack TUBG1 and exclusively express TUBG2. Using CETSA in these engineered U2OS cells, we assessed the stabilization of TUBG2 against thermal denaturation.<sup>34</sup> Western blot analysis revealed that TUBG1 and TUBG2 aggregated at different temperatures, with aggregation occurring at 55°C and 49°C in *TUBG1*-sgRNA-U2OS-TUBG1 and *TUBG1*-sgRNA-U2OS-TUBG2 cells, respectively (Figure 5C). Notably, L12 thermostabilized TUBG1 in *TUBG1*-sgRNA-U2OS-TUBG1 cells but did not stabilize TUBG2 in *TUBG1*-sgRNA-U2OS-TUBG2 cells (Figure 5D). Interestingly, we observed a reduction in TUBG2 levels with increasing concentrations of L12 in *TUBG1*-sgRNA-U2OS-TUBG2 cells. This decrease may result from cellular stress induced by higher L12 concentrations, which, as reported in this study, can affect microtubules and alter the activity of several kinases. These findings demonstrate that L12 specifically binds to TUBG1, while the observed effects on TUBG2 levels at higher L12 concentrations are likely due to off-target effects of the compound.

### 3.11 | Exploring the binding pocket of L12 on TUBG1

To identify the likely L12-binding pocket on TUBG1, we first utilized the pyKVFinder method on either the

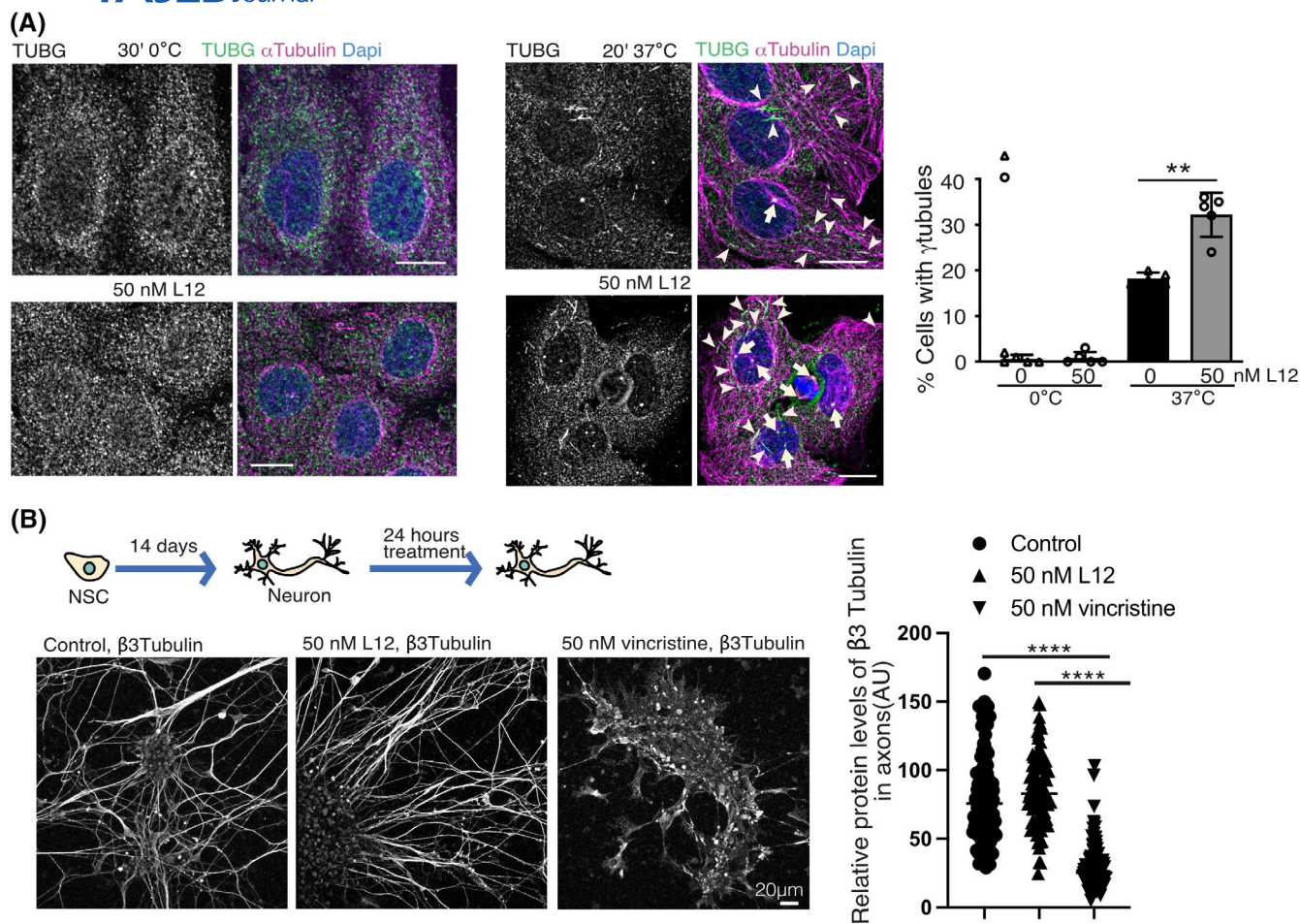


**FIGURE 4** L12 stabilizes  $\gamma$ -tubule without affecting axonal integrity. (A) Confocal microscope images display U2OS cells exposed to cold treatment, immediately fixed and stained (0 min), or treated with warm medium containing either DMSO (vehicle) or 50 nM L12. The images demonstrate that  $\gamma$ -tubules disassemble during the cold treatment and are reassembled after a 20-min incubation at 37°C. Cells were immunofluorescently labeled using anti-TUBG and  $\alpha$ -tubulin antibodies. The key finding is the mean percentage of cells with  $\gamma$ -tubules post 30-min cold treatment in the presence of 50 nM L12, followed by a 20-min incubation at 37°C. This is illustrated in the accompanying graph ( $N = 5$ ; Student's  $t$  test,  $**p < .01$ ). For each sample, a minimum of 100 cells was assessed. Scale bars: 10  $\mu$ m. Arrowheads and arrows serve to denote  $\gamma$ -tubules and centrosomes, respectively. (B) Z-stacks images present an average intensity projection of sequential 1- $\mu$ m interval images from human H9 neural stem cells (NSC) differentiated into neurons over 14 days. These cells were treated with 50 nM L12 or 50 nM vincristine for 24 h. After fixation, they were immunofluorescently labeled using an anti- $\beta$ 3-tubulin antibody, which acts as a neural axon and neural differentiation marker. The graph illustrates the mean value of the  $\beta$ 3-tubulin signal in axons ( $N = 5$ ; Student's  $t$  test,  $****p < .0001$ ).

X-ray structure or predicted 3D models of TUBG1. While these predicted 3D structures closely resembled the X-ray counterparts, they incorporated a few predicted loops absent in the experimental structure. When analyzing these 3D structures for pocket identification, we found only one pocket: the cavity responsible for binding GTP (Figure 6A).

Following this step, we applied the pocket prediction method to ten representative conformations of simulated TUBG1 using the ExProSe package. As often observed in proteins (i.e., flexible molecular objects), in several simulated structures, an additional binding pocket was revealed. This newly identified pocket aligned with

the region recognized as the colchicine-binding site or nocodazole-binding site within the  $\alpha$ -tubulin and  $\beta$ -tubulin structures (Figure 6A).

Upon superimposing the one selected simulated TUBG1 structure onto the X-ray structure of  $\beta$ -tubulin (obtained from PDB file 7Z2P) bound to nocodazole, the potential for a small molecule to bind within this TUBG1 region appeared possible.<sup>62</sup> Furthermore, L12 exhibits some structural similarities to inhibitors targeting the colchicine-binding site, such as nocodazole. Docking studies using Smina with the simulated TUBG1 structure were then performed and suggested reasonable fitting of L12 in this cryptic pocket (score  $\sim -7$  kcal/mol).

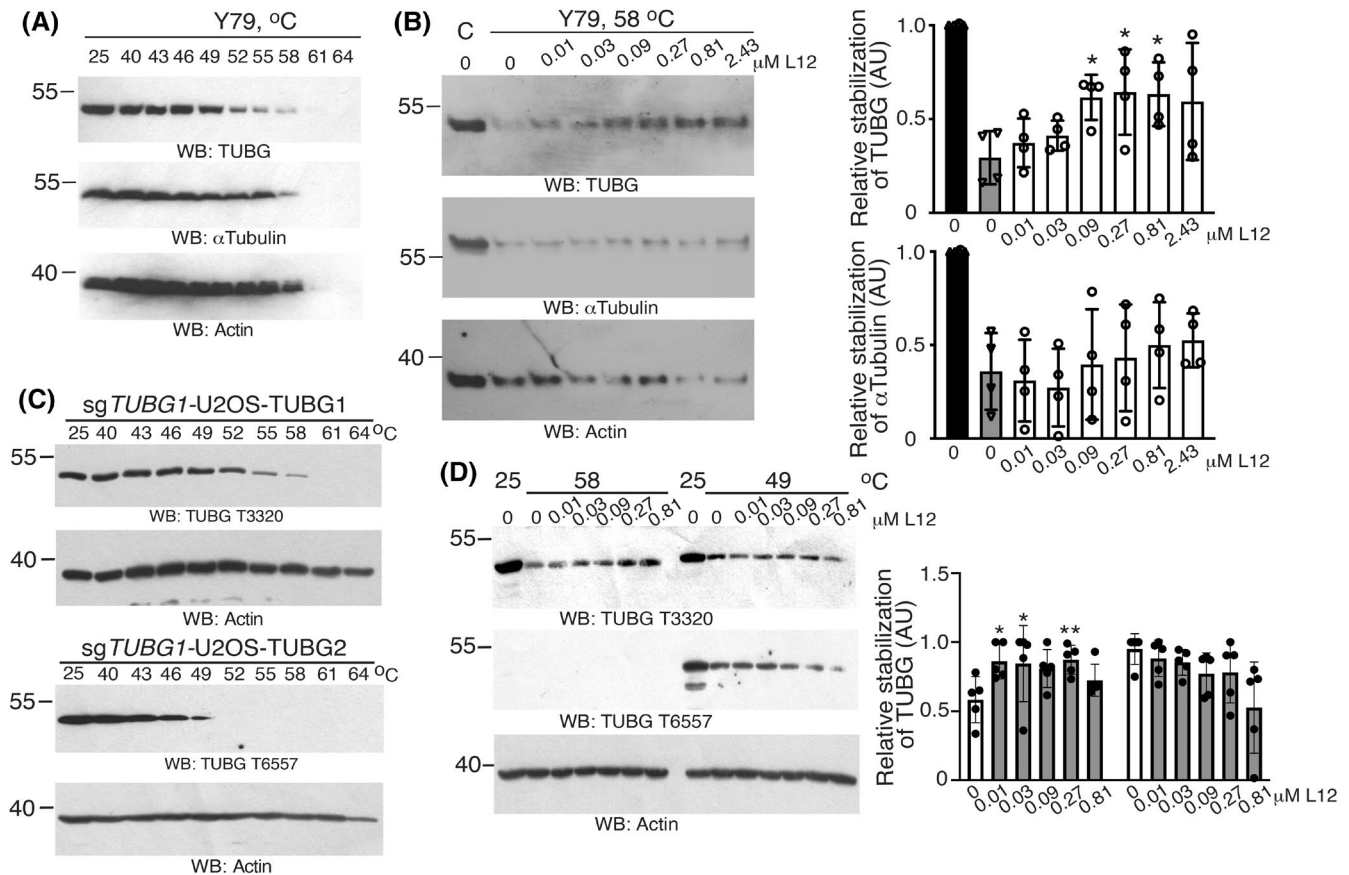


**FIGURE 5** L12 stabilizes TUBG1 against thermal denaturation. (A) Cellular thermodynamic stabilization of TUBG,  $\alpha$ -tubulin, and actin were assessed in live Y79 cells. These cells underwent a temperature gradient, and the levels of soluble TUBG,  $\alpha$ -tubulin, and actin were subsequently examined using western blot analysis with the specific antibodies. (B) After a 30 min pre-treatment of Y79 cells with DMSO or varying L12 concentrations, ligand-binding alterations in heat-induced TUBG precipitation were observed via western blotting. The specificity of L12 binding to TUBG1 was confirmed by using anti- $\alpha$ -tubulin and -actin antibodies. Note that the protein levels of  $\alpha$ -tubulin and actin were not significantly affected by L12. Graphs show densitometric analysis of the changes in the TUBG and  $\alpha$ -tubulin levels post heat-induced precipitation, normalized to the 25°C control set as 1 ( $N=4$ ). (C) Live U2OS cells stably expressing *TUBG1* sgRNA (*sgTUBG1*) and co-expressing either a sg-resistant *TUBG1* (*TUBG1*-sgRNA-U2OS-TUBG1) or *TUBG2*/*TUBG1*-sgRNA-U2OS-TUBG2), were subjected to a temperature gradient. Soluble levels of TUBG1, TUBG2, and actin post-gradient were evaluated using anti-TUBG (T3320, recognized TUBG1; T6557, recognized TUBG2) and anti-actin antibodies in western blot analysis. (D) Following a 30 min pre-treatment of *TUBG1*-sgRNA-U2OS-TUBG1 and *TUBG1*-sgRNA-U2OS-TUBG2 cells with DMSO or various concentrations of L12, ligand-induced changes in heat-induced TUBG precipitation were monitored. Graph illustrates variations in soluble TUBG1 and TUBG2 levels post heat-induced precipitation as measured by densitometric analysis of the TUBG protein content in the western blot membranes. The data were normalized to untreated cells (set as 1;  $N=4$ ; Student's *t* test, \* $p < .05$ , \*\* $p < .01$ ).

Within this identified region, residues Gln<sup>167</sup>, Asn<sup>251</sup>, and Leu<sup>321</sup> emerged as potential key players in L12 binding (Figure 6B).<sup>63</sup>

### 3.12 | Glutamine 167, asparagine 251, and leucine 321 affect L12 binding to TUBG

Gln<sup>167</sup>, Asn<sup>251</sup>, and Leu<sup>321</sup> are conserved in TUBG2 (Figures 3A and 6C). Gln<sup>167</sup> lies between the fourth  $\alpha$ -helix and the fifth parallel  $\beta$ -strand of TUBG1, three amino acids upstream of Val<sup>171</sup>, an amino acid involved

in GTP binding.<sup>18</sup> Asn<sup>251</sup> lies just before the amino acid Asp<sup>252</sup>, which in  $\alpha$ -tubulin stimulates the GTPase activity of  $\beta$ -tubulin.<sup>18,64</sup> Leu<sup>321</sup> lies between the GTPase and the DNA-binding domains (Figure 6C).

To investigate whether the binding of L12 with TUBG1 was mediated by Gln<sup>167</sup>, Asn<sup>251</sup>, and Leu<sup>321</sup>, we conducted experiments using *TUBG1*-sgRNA-U2OS. These cells were genetically engineered to stably express either the wild-type *TUBG1* gene or one of the non-reactive Ala<sup>167</sup>-, Ala<sup>251</sup>-, and Ala<sup>321</sup>-sg-resistant *TUBG1* genes (Figure 6C). Notably, while the silencing of the *TUBG1* gene or introducing mutations that compromise the TUBG-GTPase



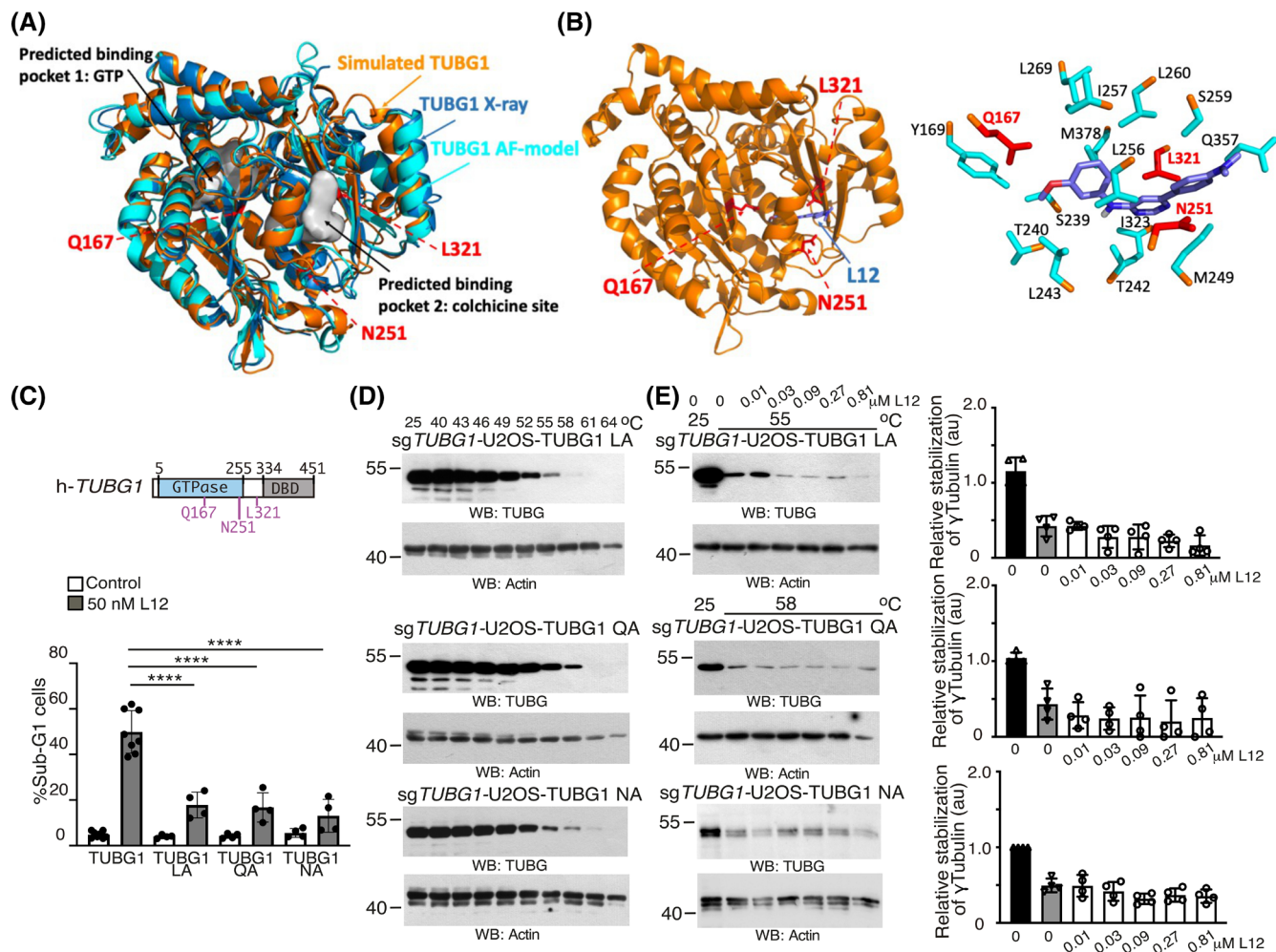


**FIGURE 6** Influence of leucine 321, glutamine 167, and asparagine 251 on L12 binding to TUBG. (A and B) Cartoon representation of the following TUBG1 structure: Simulated (mustard-yellow), X-ray (dark blue) and Alpha-Fold (AF; light blue). The structures depict the predicted binding pocket of GTP and colchicine with a view down the L12-binding pocket, highlighting the residues predicted to interact with L12. (B) L12 (blue) is shown in a stick representation at the colchicine-binding site. A close view of the binding pocket, with approximately the same orientation, shows the side chains of residues predicted to interact with L12 (best energy pose). The C-alpha atoms, when visible, are colored orange, while the remaining side chain atoms are colored cyan. The mutated residues are shown in red. (C) The illustration provided delineates the GTPase domain (residues 5–255) and the DNA-binding domain (DBD; residues 334–451) of the human *TUBG1* (h-*TUBG1*) gene. The magenta letters in the depiction denote residues comprised in the colchicine binding pocket interacting with L12 (Q167, N251 and L321). *TUBG1*-sgRNA-U2OS-TUBG1, *TUBG1*-sgRNA-U2OS-TUBG1-Ala<sup>321</sup> (LA), *TUBG1*-sgRNA-U2OS-TUBG1-Ala<sup>167</sup> (QA), and *TUBG1*-sgRNA-U2OS-TUBG1-Ala<sup>251</sup> (NA) cells were treated with 50 nM L12 for 24 h. Changes in the cell cycle profiles and the accumulation of cells in the sub-G1 phase were analyzed by determining the DNA content of cells using a nuclear counter (histograms). The graph presents the mean  $\pm$  SD of the percentage of cells in the sub-G1 fraction ( $N=4$ ; Student's *t* test, \*\*\*\* $p < .0001$ ). (D and E) The thermodynamic stabilization of TUBG and actin was examined in live *TUBG1*-sgRNA-U2OS-TUBG1-Ala<sup>321</sup> (LA), *TUBG1*-sgRNA-U2OS-TUBG1-Ala<sup>167</sup> (QA), and *TUBG1*-sgRNA-U2OS-TUBG1-Ala<sup>251</sup> (NA) cells. Cell populations underwent a temperature gradient ( $^{\circ}\text{C}$ ) or were exposed to specific temperatures post 30-min L12 pre-treatment (D). Subsequently, soluble levels of TUBG and actin were determined using western blot analysis with respective antibodies. Graphs in section D depict changes in the soluble TUBG levels post heat-induced precipitation, with data normalized to a 25 $^{\circ}\text{C}$  control set as 1 ( $N=4$ ).

domain typically has detrimental effects on cells, our modified cell lines appeared to thrive and did not exhibit adverse reactions upon L12 treatment.

Our findings revealed that the inhibitory effect of L12 on TUBG1 was markedly reduced in cell lines expressing the mutated TUBG1 variants (Ala<sup>167</sup>-, Ala<sup>251</sup>- or Ala<sup>321</sup>-TUBG1)

along with *TUBG1*-sgRNA. This observation underscored the critical role of these specific residues in mediating the binding of L12 to TUBG1 (Figure 6C).

Moreover, we also tested a possible direct binding of L12 to TUBG1 mutants in live cells by testing the effect of L12 on the stabilization of the mutants against thermal



denaturation in *TUBG1*-sgRNA-U2OS-TUBG1- Ala<sup>167</sup>, -Ala<sup>251</sup>, and -Ala<sup>321</sup> cells<sup>34</sup> and the resulting levels of soluble TUBG were assessed by western blot (Figure 6D,E). It is worth noting that the mutants aggregated at 55°C (TUBG1-Ala<sup>321</sup>) and 58°C (TUBG1-Ala<sup>167</sup> and -Ala<sup>251</sup>) (Figure 6D). Examination of *TUBG1*-sgRNA-U2OS-TUBG1- Ala<sup>167</sup>, -Ala<sup>251</sup>, and -Ala<sup>321</sup> cells after treatment with L12 showed that L12 thermostabilized neither of the mutants (Figure 6E), confirming the importance of these residues for L12 binding.

### 3.13 | Higher concentrations of L12 affect microtubule dynamics

The protein sequence of TUBG exhibits 54% and 57% homology with the sequences in  $\alpha$ - (AAA91576.1) and  $\beta$ -tubulin (AAC52035.1), respectively. Due to the similarities between  $\alpha$ -,  $\beta$ -tubulin, and TUBG, and the function of TUBG in the nucleation of  $\alpha\beta$ -tubulin dimers,<sup>18</sup> we sought to analyze possible effects of L12 on  $\alpha\beta$ -tubulin dynamics with an astral MT regrowth assay in U2OS, *TUBG1*-sgRNA-U2OS-TUBG1, and *TUBG1*-sgRNA-U2OS-TUBG2 cells (Figure 7A–C).<sup>65</sup> Immunofluorescence staining showed that colcemid treatment (a known MT destabilizing agent) abolished MT regrowth in the three cell lines (Figure 7A–C). Furthermore, treatment with 100 nM of L12 diminished MT regrowth in the same cells, but MT regrowth was unaffected at 10 nM of L12 (Figure 7A–C). These observations indicate that L12 may interfere with astral microtubule outgrowth when used at higher concentrations. It also demonstrates that the increased cytotoxicity of L12 in cells expressing TUBG1 did not depend on the functions of TUBG in the regulation of microtubule dynamics, as L12 showed the same effect on astral microtubule outgrowth in U2OS, *TUBG1*-sgRNA-U2OS-TUBG1, and *TUBG1*-sgRNA-U2OS-TUBG2 cells (Figure 7A–C). This result is consistent with L12 binding at the colchicine binding pocket of  $\beta$ -tubulin, further supporting the compound's potential to disrupt microtubule dynamics at higher concentrations.

### 3.14 | L12 treatment delays xenograft tumor growth in tumor cells with an impaired RB1 pathway

To study the effect of L12 on tumor growth, we performed an experiment using mice that were implanted with U1690 (lacks RB1 expression, Figures 1B and 8). We found that L12 itself was well tolerated compared to the vehicle group and that L12 significantly interfered with tumor growth in the treated animals (Figure 8). Moreover, the xenografted

U1690 cells formed fast-growing heterogeneous tumors, and given the size of the tumors, three mice in the control group and one mouse in the treated group had to be sacrificed before the end of the experiment. Altogether, these data demonstrate that inhibition of TUBG1 can be considered a new target for cancer treatment.

## 4 | DISCUSSION

The present study offers a compelling exploration into the potential of targeting TUBG1 as a therapeutic approach in cancer treatment. The significance of microtubules in cellular dynamics and their disruption as a strategy for tumor eradication is well established. However, the associated toxicities, due to the targeting of both malignant and healthy cells, have been a major concern, making it imperative the search for more selective therapies.

Our findings introduce L12 as a promising candidate. Here, we demonstrate that L12 is cytotoxic to cells lacking a functional RB1 pathway, with its cytotoxicity dependent on the protein levels of TUBG1, E2F1, and RB1. Notably, L12 affects the thermodynamic stabilization of TUBG1 without impacting TUBG2, distinguishing it from other TUBG inhibitors.<sup>16,17,66</sup> Unlike traditional TUBG-targeting agents, L12 demonstrates specificity for tumor cells by inhibiting TUBG1 without affecting TUBG2. This selectivity is crucial as it potentially minimizes adverse effects on healthy tissues, particularly in the case of neuropathy,<sup>61</sup> since TUBG2 expression may compensate for the loss of TUBG1 function, addressing a common limitation of current therapies. This study highlights L12's potential as a targeted therapeutic agent, emphasizing its ability to enhance RB1 expression and selectively target cells with impaired RB1 signaling.<sup>13</sup>

Further supporting the selectivity of L12, our study indicates that reducing TUBG1 levels enhances L12's cytotoxic effects, potentially by altering the balance between free and L12-bound TUBG1. A plausible explanation is that as TUBG1 levels decrease, the proportion of TUBG1 molecules engaged in complexes with L12 increases, thereby limiting TUBG1 availability for other functional interactions. One possible consequence of this shift is a competition between TUBG1-L12 complexes and RB1 for binding to E2F1, which could disrupt the regulatory influence of RB1 and ultimately contribute to increased cellular toxicity, as observed in MCF10A cells with reduced levels of TUBG1. The restoration of cellular resistance upon the re-introduction of functional TUBG1 further supports this interpretation. Although the direct formation of TUBG1-L12 complexes under these conditions was not measured, these findings suggest a mechanistic link between TUBG1 expression levels, RB1 regulation, and L12's cytotoxicity.<sup>13,14</sup>

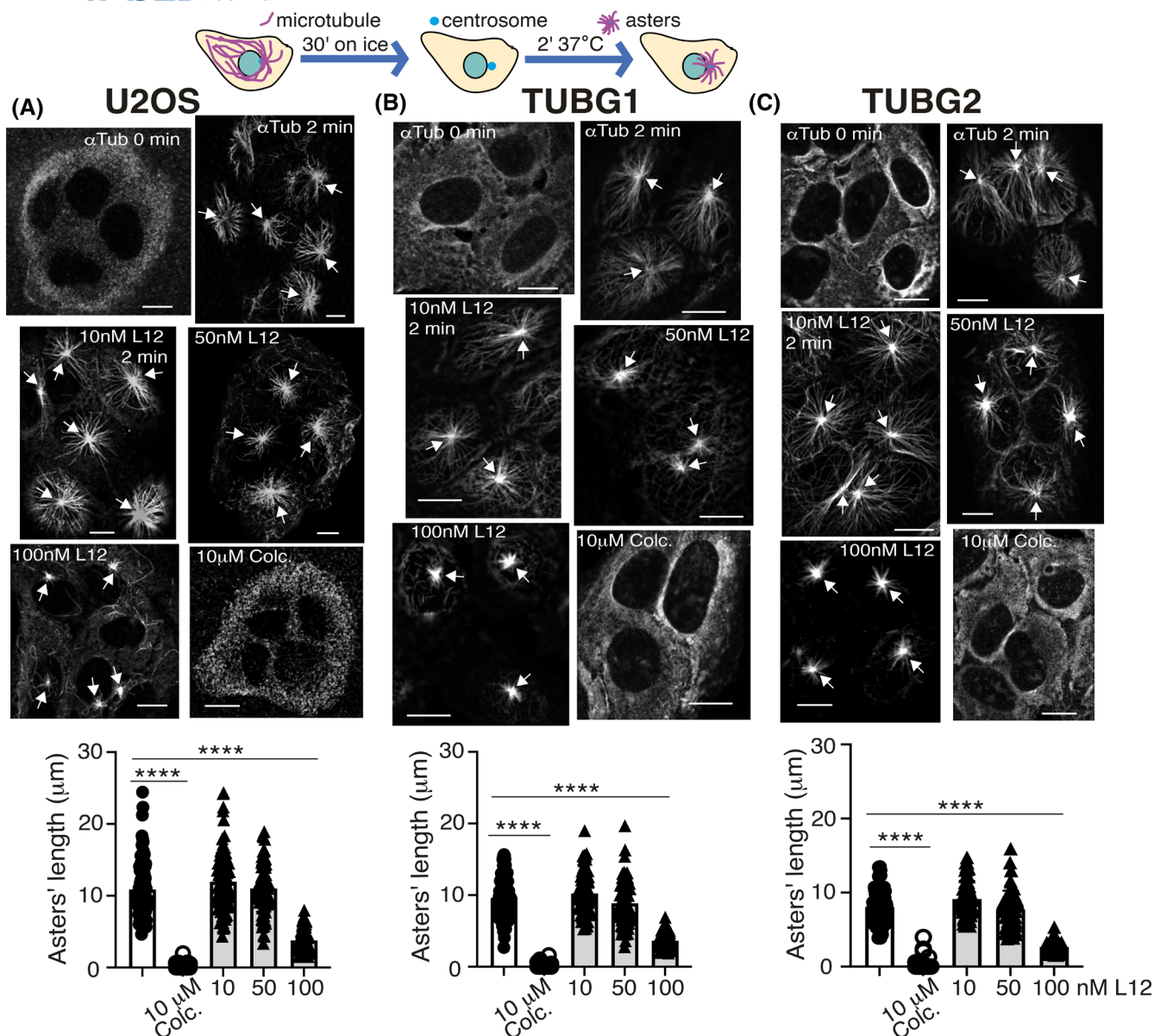


**FIGURE 7** Impact of L12 on microtubule outgrowth. (A–C) U2OS cells (A) or those stably co-expressing *TUBG*-sgRNA and either *TUBG1* (B) or a *TUBG2* (C) sg-resistant were subjected to cold treatment. Subsequently, these cells were either immediately stained (0 min) or stained 2 min after the addition of warm medium supplemented with: 2 μL/mL DMSO (vehicle), 10 μM colcemid (Colc.; known to inhibit microtubule regrowth), or in the presence of various concentrations of L12, as specified. After treatment, cells were fixed and subjected to immunofluorescence labeling with an anti- $\alpha$ -tubulin antibody. Scale bars are indicated as 10 μm. Arrows indicate astral microtubule regrowth from centrosomes. The graphs display the average aster length measured with ImageJ (Fiji, [RRID:SCR\\_003070](https://doi.org/10.1002/ajb.10000)) software<sup>33</sup> in U2OS cells (A;  $N=100$ ) and in those stably co-expressing *TUBG*-sgRNA with either *TUBG1* (B;  $N=100$ ) or *TUBG2* (C;  $N=100$ ). Statistical analysis was conducted using Student's *t* test, with significance denoted as \*\*\*\* $p < .0001$ .

At concentrations twice those needed for cytotoxicity in tumor cells, L12 treatment exhibits a trend toward thermodynamic stabilization of  $\alpha\beta$ -tubulin. The effects on astral microtubule outgrowth are observed across all cell lines studied, independent of the expression of *TUBG1* or *TUBG2* isoforms. This implies that the cytotoxic effects of L12 on cells are not caused by impairment of microtubule dynamics but are instead dependent on the inhibition of the nuclear activities of *TUBG1*. Consistent with this

concept, the eleven amino acids that differentiate *TUBG1* from *TUBG2* cause the unique conformations of the isoforms.<sup>20</sup> These conformational differences contribute to *TUBG2*'s reduced nuclear localization and the diminished toxicity of L12 in cells expressing *TUBG2*, underscoring the importance of *TUBG1*'s specific nuclear functions for L12's cytotoxic effect.

Although L12's  $\gamma$ -tubule-stabilizing properties are not the primary mechanism of selective cytotoxicity in

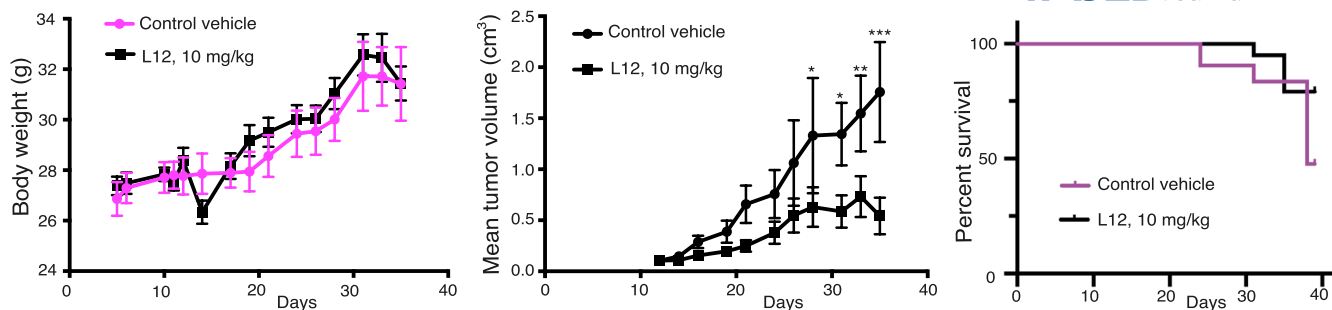


**FIGURE 8** L12 effect on tumor growth of xenografted U1690 mice. Left represents the changes in body weight of mice xenografted with U1690 cells during treatment. The middle shows tumor growth in xenografted U1690 cells treated three days per week with a dosage of 20 mg/kg L12. L12 treatment started on day 12 when the tumors reached a mean tumor volume of 100 mm<sup>3</sup>. (two-way ANOVA, \* $p < .05$ , \*\* $p < .01$ , \*\*\* $p < .001$ ,  $N = 8$  mice per group). As the xenografted tumor surpassed a tumor volume of 1 cm<sup>3</sup>, three mice from the control group and one mouse in the L12-treated group were sacrificed, as indicated.

RB1-deficient cells, these effects are important for visualizing how L12 acts on cellular structures and for understanding its broader impact. The ability to form  $\gamma$ -tubules is reduced in TUBG2-expressing cells compared to TUBG1-expressing cells. This, combined with the observation of reduced L12 toxicity in cells expressing only TUBG2, as opposed to TUBG1, suggests that  $\gamma$ -tubule formation may be a key factor influencing the degree of L12's cytotoxicity. The polymerizing traits of the TUBG meshwork in the nucleus, while not fully understood, appear critical for its nuclear functions. These polymerization dynamics may influence how TUBG interacts with nuclear factors, including E2F1, which may be relevant for regulating apoptosis in response to L12 treatment.

Importantly, our findings provide a foundation for exploring the applicability of L12 in other cancer types with similar molecular profiles, particularly those with nonfunctional RB1. RB pathway deficiencies are observed in a wide range of malignancies, including retinoblastoma, small cell lung cancer, triple-negative breast cancer, glioblastoma, and bladder cancer, among others.<sup>50,67–70</sup> The frequent loss of RB1 in these tumor types often correlates with poor clinical outcomes and resistance to conventional therapies, highlighting the urgent need for novel therapeutic strategies.<sup>71</sup> Given L12's selective cytotoxicity in RB1-deficient cancer cells and its ability to enhance RB1 expression, it has the potential to be effective across multiple tumor types that share this molecular feature.

L12's unique mechanism of action becomes particularly evident in comparison with other TUBG-targeting agents. Gatastatin, for example, prevents microtubule nucleation by blocking the  $\gamma$ TuRC,<sup>66</sup> while CDA binds to the GTPase domain of TUBG,<sup>16,17</sup> acting as a depolymerizing agent.<sup>2</sup> This makes L12 distinct among TUBG inhibitors,

as it selectively targets cancer cells with impaired RB1 signaling pathways.

L12 was identified within a kinase-focused compound collection. Previous studies have demonstrated that kinase inhibitors can bind to both  $\alpha$ -tubulin and  $\beta$ -tubulin.<sup>72</sup> Conversely, nocodazole, a tubulin inhibitor that binds to the colchicine-binding site, induces microtubule depolymerization while also displaying affinities for multiple kinases like ABL, c-KIT, BRAF, and MEK.<sup>40</sup> In this context, we highlight L12's potential, noting its affinity for KITD816V, MAP4K5, and MAPKAPK2 kinases, and its direct interaction with TUBG1 at the colchicine binding site. Moreover, the detailed analysis presented of the binding pockets and specific residues involved in L12-TUBG interaction provides critical insights for further drug development.

The promising results of L12 in inhibiting tumor growth in xenografted small cell lung cancer cells underscore its potential therapeutic efficacy. Furthermore, the reduced neuronal axonal toxicity of L12 compared to vincristine adds to its therapeutic appeal. These findings pave the way for exploring L12's clinical applicability while addressing the safety concerns associated with current treatments.

In conclusion, this study highlights the potential of TUBG1 inhibitors like L12 as a targeted therapeutic approach aligned with personalized chemotherapy principles, addressing the molecular profiles of tumors with RB1 pathway deficiencies. The demonstrated selectivity of L12 in targeting RB1-deficient cancers suggests that it could be applied to a broad spectrum of malignancies with similar molecular vulnerabilities, offering new hope for improving patient outcomes in difficult-to-treat cancers. Continued research and clinical trials will be essential to fully realize L12's therapeutic potential and further refine cancer treatment paradigms.



## AUTHOR CONTRIBUTIONS

*Conception and design:* M. Alvarado-Kristensson. *Development of methodology:* L. Lindström, B. O. Villoutreix, T. M. Otrocka, Lundbäck, M. Alvarado-Kristensson. *Collection and assembly of data:* L. Lindström, J. Zhou, D. Malycheva, M. Otrocka, M. Anwar Shameem, D. Bliman, M. Straw, K. Riesbeck, R. Olsson, M. Alvarado-Kristensson. *Chemistry:* M. Anwar Shameem, D. Bliman, R. Olsson. *Analysis and interpretation of data (e.g., computational analysis, identification and selection of compounds):* L. Lindström, J. Zhou, B. O. Villoutreix, M. Otrocka, Anna-Lena Gustavsson, R. Olsson, and M. Alvarado-Kristensson. *Paper writing:* L. Lindström, J. Zhou, B. O. Villoutreix, M. Otrocka, A. L. Gustavsson, R. Olsson, and M. Alvarado-Kristensson. All authors have read and approved the article.

## ACKNOWLEDGMENTS

We thank William Sellers (Broad Institute), Kristian Helin (Biotech Research & Innovation Centre), Feng Zhang (Massachusetts Institute of Technology) Joseph R. Nevins (Duke University), Antoine Royant (Institut de Biologie Structurale), William Gerwick (Skaggs school of Pharmacy and Pharmaceutical Sciences) and Lucie Karayan-Tapon (Poitiers University Hospital) for reagents.

During the preparation of this work, the authors used ChatGPT to improve language clarity. After using this tool, the authors carefully reviewed and edited the content as needed and took full responsibility for the final publication.

## FUNDING INFORMATION

This work was supported by the Swedish Cancer Society (222176Pj), the Swedish Childhood Cancer Fund (PR2022-0058), BioCare (2012), Novo Nordisk foundation (12759), MultiPark (the Lund University Strategic Research Areas), Skåne University Hospital in Malmö Cancer Research Fund, and Sten K. Johnson's Stiftelse (2022). CBCS is a national research infrastructure funded by the Swedish Research Council (dr.nr.2021-00179) and SciLifeLab ([www.scilifelab.se](http://www.scilifelab.se)).


## DISCLOSURES

The authors declare no competing interests.

## DATA AVAILABILITY STATEMENT

The data that support the findings of this study are available on request from the corresponding author.

## ORCID

Lisa Lindström  <https://orcid.org/0009-0008-4510-4635>  
Jingkai Zhou  <https://orcid.org/0000-0002-9867-3486>  
Bruno O. Villoutreix  <https://orcid.org/0000-0002-6456-7730>

Magdalena Otrocka  <https://orcid.org/0000-0002-2139-8236>

Anna-Lena Gustavsson  <https://orcid.org/0000-0003-4332-2336>

Thomas Lundbäck  <https://orcid.org/0000-0002-8145-7808>

David Bliman  <https://orcid.org/0000-0003-0487-8366>

Muhammad Anwar Shameem  <https://orcid.org/0000-0001-6173-3417>

Kristian Riesbeck  <https://orcid.org/0000-0001-6274-6965>

Roger Olsson  <https://orcid.org/0000-0002-7107-3472>

Maria Alvarado-Kristensson  <https://orcid.org/0000-0003-0598-7986>

## REFERENCES

1. Zhou J, Giannakakou P. Targeting microtubules for cancer chemotherapy. *Curr Med Chem Anticancer Agents*. 2005;5: 65-71.
2. Lindstrom L, Alvarado-Kristensson M. Characterization of gamma-tubulin filaments in mammalian cells. *Biochim Biophys Acta*. 2018;1865:158-171.
3. Lindstrom L, Li T, Malycheva D, et al. The GTPase domain of gamma-tubulin is required for normal mitochondrial function and spatial organization. *Commun Biol*. 2018;1:37.
4. Rossello CA, Lindstrom L, Eklund G, Corvaisier M, Kristensson MA. Gamma-tubulin–gamma-tubulin interactions as the basis for the formation of a meshwork. *Int J Mol Sci*. 2018;19:3245.
5. Malycheva D, Alvarado-Kristensson M. Molecular characterization of the TUBG1 meshwork's influence on cytoskeletal organization. *Heliyon*. 2025;11:e41829.
6. Sulimenko V, Draberova E, Draber P. Gamma-tubulin in microtubule nucleation and beyond. *Front Cell Dev Biol*. 2022;10:880761.
7. Findeisen P, Muhlhausen S, Dempewolf S, et al. Six subgroups and extensive recent duplications characterize the evolution of the eukaryotic tubulin protein family. *Genome Biol Evol*. 2014;6:2274-2288.
8. Poirier K, Lebrun N, Broix L, et al. Mutations in TUBG1, DYNC1H1, KIF5C and KIF2A cause malformations of cortical development and microcephaly. *Nat Genet*. 2013;45:639-647.
9. Rossello CA, Lindstrom L, Glindre J, Eklund G, Alvarado-Kristensson M. Gamma-tubulin coordinates nuclear envelope assembly around chromatin. *Heliyon*. 2016;2:e00166.
10. Malycheva D, Alvarado-Kristensson M. Centrosome movements are TUBG1-dependent. *Int J Mol Sci*. 2023;24(17):13154. doi:10.3390/ijms241713154
11. Alvarado-Kristensson M. Gamma-tubulin as a signal-transducing molecule and meshwork with therapeutic potential. *Signal Transduct Target Ther*. 2018;3:24.
12. Alvarado-Kristensson M. Choreography of the centrosome. *Heliyon*. 2020;6:e03238.
13. Ehlen A, Rossello CA, von Stedingk K, et al. Tumors with nonfunctional retinoblastoma protein are killed by reduced gamma-tubulin levels. *J Biol Chem*. 2012;287:17241-17247.
14. Hoog G, Zarri R, von Stedingk K, Jonsson K, Alvarado-Kristensson M. Nuclear localization of gamma-tubulin affects



- E2F transcriptional activity and S-phase progression. *FASEB J*. 2011;25:3815-3827.
15. Corvaisier M, Alvarado-Kristensson M. Non-canonical functions of the gamma-tubulin meshwork in the regulation of the nuclear architecture. *Cancers (Basel)*. 2020;12(11):3102. doi:10.3390/cancers12113102
  16. Lindstrom L, Villoutreix BO, Lehn S, et al. Therapeutic targeting of nuclear gamma-tubulin in RB1-negative tumors. *Mol Cancer Res*. 2015;13:1073-1082.
  17. Lindstrom L, Villoutreix BO, Lehn S, et al. Editor's note: therapeutic targeting of nuclear gamma-tubulin in RB1-negative tumors. *Mol Cancer Res*. 2024;22:1064.
  18. Kristensson MA. The game of tubulins. *Cells*. 2021;10(4):745. doi:10.3390/cells10040745
  19. Alvarado-Kristensson M, Rodriguez MJ, Silio V, Valpuesta JM, Carrera AC. SADB phosphorylation of gamma-tubulin regulates centrosome duplication. *Nat Cell Biol*. 2009;11:1081-1092.
  20. Corvaisier M, Zhou J, Malycheva D, et al. The gamma-tubulin meshwork assists in the recruitment of PCNA to chromatin in mammalian cells. *Commun Biol*. 2021;4:767.
  21. Sellers WR, Novitch BG, Miyake S, et al. Stable binding to E2F is not required for the retinoblastoma protein to activate transcription, promote differentiation, and suppress tumor cell growth. *Genes Dev*. 1998;12:95-106.
  22. Black EP, Hallstrom T, Dressman HK, West M, Nevins JR. Distinctions in the specificity of E2F function revealed by gene expression signatures. *Proc Natl Acad Sci USA*. 2005;102:15948-15953.
  23. Ran FA, Hsu PD, Wright J, Agarwala V, Scott DA, Zhang F. Genome engineering using the CRISPR-Cas9 system. *Nat Protoc*. 2013;8:2281-2308.
  24. Nygren P, Larsson R, Gruber A, Peterson C, Bergh J. Doxorubicin selected multidrug-resistant small cell lung cancer cell lines characterised by elevated cytoplasmic Ca<sup>2+</sup> and resistance modulation by verapamil in absence of P-glycoprotein overexpression. *Br J Cancer*. 1991;64:1011-1018.
  25. Balbous A, Cortes U, Guilloteau K, et al. A mesenchymal glioma stem cell profile is related to clinical outcome. *Oncogenesis*. 2014;3:e91.
  26. Alvarado-Kristensson M, Porn-Ares MI, Grethe S, Smith D, Zheng L, Andersson T. p38 mitogen-activated protein kinase and phosphatidylinositol 3-kinase activities have opposite effects on human neutrophil apoptosis. *FASEB J*. 2002;16:129-131.
  27. Bednarska I, Malycheva D, Kristensson MA. Complete solubilization of mammalian cells in lysates. *MethodsX*. 2024;13:102860.
  28. Zhou J, Alvarado-Kristensson M. Optimization of production of recombinant gamma-tubulin in bacteria. *MethodsX*. 2021;8:101517.
  29. Muller H, Bracken AP, Vernell R, et al. E2Fs regulate the expression of genes involved in differentiation, development, proliferation, and apoptosis. *Genes Dev*. 2001;15:267-285.
  30. Kim M, Hwang YS, Cho W, Park SB. Synthesis of 3,5-disubstituted isoxazoles containing privileged substructures with a diverse display of polar surface area. *ACS Comb Sci*. 2017;19:407-413.
  31. Achelle S, Ramondenc Y, Marsais F, Plé N. Star- and banana-shaped oligomers with a pyrimidine core: synthesis and light-emitting properties. *Eur J Org Chem*. 2008;2008:3129-3140.
  32. Alvarado-Kristensson M. A simple and fast method for fixation of cultured cell lines that preserves cellular structures containing gamma-tubulin. *MethodsX*. 2018;5:227-233.
  33. Bolte S, Cordelieres FP. A guided tour into subcellular colocalization analysis in light microscopy. *J Microsc*. 2006;224:213-232.
  34. Jafari R, Almqvist H, Axelsson H, et al. The cellular thermal shift assay for evaluating drug target interactions in cells. *Nat Protoc*. 2014;9:2100-2122.
  35. Aldaz H, Rice LM, Stearns T, Agard DA. Insights into microtubule nucleation from the crystal structure of human gamma-tubulin. *Nature*. 2005;435:523-527.
  36. Jumper J, Evans R, Pritzel A, et al. Highly accurate protein structure prediction with AlphaFold. *Nature*. 2021;596:583-589.
  37. Waterhouse A, Bertoni M, Bienert S, et al. SWISS-MODEL: homology modelling of protein structures and complexes. *Nucleic Acids Res*. 2018;46:W296-W303.
  38. Greener JG, Filippis I, Sternberg MJE. Predicting protein dynamics and Allostery using multi-protein atomic distance constraints. *Structure*. 2017;25:546-558.
  39. de la Roche NM, Muhlethaler T, Di Martino RMC, et al. Novel fragment-derived colchicine-site binders as microtubule-destabilizing agents. *Eur J Med Chem*. 2022;241:114614.
  40. Park H, Hong S, Hong S. Nocodazole is a high-affinity ligand for the cancer-related kinases ABL, c-KIT, BRAF, and MEK. *ChemMedChem*. 2012;7:53-56.
  41. Guerra J, Ribeiro-Filho HV, Jara GE, Bortot LO, Pereira JGC, Lopes-de-Oliveira PS. pyKVFinder: an efficient and integrable Python package for biomolecular cavity detection and characterization in data science. *BMC Bioinform*. 2021;22:607.
  42. Lagorce D, Bouslama L, Becot J, Miteva MA, Villoutreix BO. FAF-Drugs4: free ADME-tox filtering computations for chemical biology and early stages drug discovery. *Bioinformatics*. 2017;33:3658-3660.
  43. Bruns RF, Watson IA. Rules for identifying potentially reactive or promiscuous compounds. *J Med Chem*. 2012;55:9763-9772.
  44. Koes DR, Baumgartner MP, Camacho CJ. Lessons learned in empirical scoring with smina from the CSAR 2011 benchmarking exercise. *J Chem Inf Model*. 2013;53:1893-1904.
  45. Trott O, Olson AJ. AutoDock Vina: improving the speed and accuracy of docking with a new scoring function, efficient optimization, and multithreading. *J Comput Chem*. 2010;31:455-461.
  46. Quiroga R, Villarreal MA. Vinardo: a scoring function based on Autodock Vina improves scoring, docking, and virtual screening. *PLoS One*. 2016;11:e0155183.
  47. Bjerrum EJ. Machine learning optimization of cross docking accuracy. *Comput Biol Chem*. 2016;62:133-144.
  48. Fuentes N, Silva Rodriguez M, Silveyra P. Role of sex hormones in lung cancer. *Exp Biol Med*. 2021;246:2098-2110.
  49. Miczek KA, Maxson SC, Fish EW, Faccidomo S. Aggressive behavioral phenotypes in mice. *Behav Brain Res*. 2001;125:167-181.
  50. Chen HZ, Tsai SY, Leone G. Emerging roles of E2Fs in cancer: an exit from cell cycle control. *Nat Rev Cancer*. 2009;9:785-797.
  51. Molenaar JJ, Ebus ME, Koster J, et al. Cyclin D1 and CDK4 activity contribute to the undifferentiated phenotype in neuroblastoma. *Cancer Res*. 2008;68:2599-2609.
  52. Zhang J, Mullighan CG, Harvey RC, et al. Key pathways are frequently mutated in high-risk childhood acute lymphoblastic leukemia: a report from the Children's Oncology Group. *Blood*. 2011;118:3080-3087.
  53. Kallai BM, Kourova H, Chumova J, et al. Gamma-tubulin interacts with E2F transcription factors to regulate proliferation and endocycling in Arabidopsis. *J Exp Bot*. 2020;71:1265-1277.

54. Eklund G, Lang S, Glindre J, Ehlen A, Alvarado-Kristensson M. The nuclear localization of gamma-tubulin is regulated by SadB-mediated phosphorylation. *J Biol Chem.* 2014;289:21360-21373.
55. Park YB, Park MJ, Kimura K, Shimizu K, Lee SH, Yokota J. Alterations in the INK4a/ARF locus and their effects on the growth of human osteosarcoma cell lines. *Cancer Genet Cytogenet.* 2002;133:105-111.
56. Yoon YK, Kim HP, Han SW, et al. KRAS mutant lung cancer cells are differentially responsive to MEK inhibitor due to AKT or STAT3 activation: implication for combinatorial approach. *Mol Carcinog.* 2010;49:353-362.
57. Martelli M, Monaldi C, De Santis S, et al. Recent advances in the molecular biology of systemic mastocytosis: implications for diagnosis, prognosis, and therapy. *Int J Mol Sci.* 2020;21(11):3987. doi:10.3390/ijms21113987
58. Chuang HC, Wang X, Tan TH. MAP4K family kinases in immunity and inflammation. *Adv Immunol.* 2016;129:277-314.
59. Soni S, Anand P, Padwad YS. MAPKAPK2: the master regulator of RNA-binding proteins modulates transcript stability and tumor progression. *J Exp Clin Cancer Res.* 2019;38:121.
60. Biswas AK, Johnson DG. Transcriptional and nontranscriptional functions of E2F1 in response to DNA damage. *Cancer Res.* 2012;72:13-17.
61. Kandula T, Park SB, Cohn RJ, Krishnan AV, Farrar MA. Pediatric chemotherapy induced peripheral neuropathy: a systematic review of current knowledge. *Cancer Treat Rev.* 2016;50:118-128.
62. Lopez-Lopez E, Cerda-Garcia-Rojas CM, Medina-Franco JL. Tubulin inhibitors: a chemoinformatic analysis using cell-based data. *Molecules.* 2021;26(9):2483. doi:10.3390/molecules26092483
63. Wang Y, Zhang H, Gigant B, et al. Structures of a diverse set of colchicine binding site inhibitors in complex with tubulin provide a rationale for drug discovery. *FEBS J.* 2016;283:102-111.
64. Anders KR, Botstein D. Dominant-lethal alpha-tubulin mutants defective in microtubule depolymerization in yeast. *Mol Biol Cell.* 2001;12:3973-3986.
65. Chaimovitch D, Abu-Abied M, Belausov E, Rubin B, Dudai N, Sadot E. Microtubules are an intracellular target of the plant terpene citral. *Plant J.* 2010;61:399-408.
66. Chinen T, Liu P, Shioda S, et al. The gamma-tubulin-specific inhibitor gatastatin reveals temporal requirements of microtubule nucleation during the cell cycle. *Nat Commun.* 2015;6:8722.
67. Lee EY, Bookstein R, Young LJ, Lin CJ, Rosenfeld MG, Lee WH. Molecular mechanism of retinoblastoma gene inactivation in retinoblastoma cell line Y79. *Proc Natl Acad Sci USA.* 1988;85:6017-6021.
68. Patel JM, Goss A, Garber JE, et al. Retinoblastoma protein expression and its predictors in triple-negative breast cancer. *NPJ Breast Cancer.* 2020;6:19.
69. Chkheidze R, Raisanen J, Gagan J, et al. Alterations in the RB pathway with inactivation of RB1 characterize glioblastomas with a primitive neuronal component. *J Neuropathol Exp Neurol.* 2021;80:1092-1098.
70. Miyamoto H, Shuin T, Torigoe S, Iwasaki Y, Kubota Y. Retinoblastoma gene mutations in primary human bladder cancer. *Br J Cancer.* 1995;71:831-835.
71. de Garcia Herreros M, Jimenez N, Rodriguez-Carunchio L, et al. Prognostic expression signature of RB1, PTEN, and TP53 genes in patients with metastatic hormone-sensitive prostate cancer treated with androgen receptor pathway inhibitors. *Eur Urol Open Sci.* 2024;70:86-90.
72. Lafanechere L. The microtubule cytoskeleton: an old validated target for novel therapeutic drugs. *Front Pharmacol.* 2022;13:969183.

## SUPPORTING INFORMATION

Additional supporting information can be found online in the Supporting Information section at the end of this article.

**How to cite this article:** Lindström L, Zhou J, Villoutreix BO, et al. Targeting TUBG1 in RB1-negative tumors. *The FASEB Journal.* 2025;39:e70431. doi:10.1096/fj.202403180RR